

Log N - Log S Relations and Spectral Properties of Sources from the ASCA Large Sky Survey — their Implications for the Origin of the Cosmic X-ray Background (CXB)

Yoshihiro Ueda, Tadayuki Takahashi, and Hajime Inoue

Institute of Space and Astronautical Science, Kanagawa 229-8510, Japan
 ueda@astro.isas.ac.jp, takahashi@astro.isas.ac.jp, inoue@astro.isas.ac.jp

Takeshi Tsuru and Masaaki Sakano

Department of Physics, Kyoto University, Kyoto 606-8502, Japan
 tsuru@cr.scphys.kyoto-u.ac.jp, sakano@cr.scphys.kyoto-u.ac.jp

Yoshitaka Ishisaki

Department of Physics, Tokyo Metropolitan University, Hachioji, Tokyo 192-0397, Japan
 ishisaki@phys.metro-u.ac.jp

Yasushi Ogasaka

Department of Astrophysics, Nagoya University, Nagoya 464-8602, Japan
 ogasaka@u.phys.nagoya-u.ac.jp

Kazuo Makishima

Department of Physics, University of Tokyo, Bunkyo-ku, Tokyo 113-0033, Japan
 makima@phys.s.u-tokyo.ac.jp

Toru Yamada

Astronomical Institute, Tohoku University, Sendai 980-8578, Japan
 yamada@astr.tohoku.ac.jp

and

Masayuki Akiyama and Kouji Ohta

Department of Astronomy, Kyoto University, Kyoto 606-8502, Japan
 akiyama@kusastro.kyoto-u.ac.jp, ohta@kusastro.kyoto-u.ac.jp

ABSTRACT

We carried out the first wide-area unbiased survey with the *ASCA* satellite in the 0.7–10 keV band around a north Galactic-pole region covering a continuous area of 7 deg² (Large Sky Survey; LSS). To make the best use of *ASCA* capability, we developed a new source-detection method where the complicated detector responses are fully taken into account. Applying this method to the entire LSS data independently in the total (0.7–7 keV), hard (2–10 keV), and soft (0.7–2 keV) band, we detected 107 sources altogether with sensitivity limits of 6×10^{-14} (0.7–7 keV), 1×10^{-13} (2–10 keV), and 2×10^{-14} erg s⁻¹ cm⁻² (0.7–2 keV), respectively. A complete list of the detected sources is presented. Based on detailed studies by Monte Carlo simulations, we evaluated effects of the source confusion and accurately derived Log N - Log S relation in each survey band. The Log N - Log S relation in the hard band is located on the extrapolation from the *Ginga* and *HEAO1* results with the Euclidean slope of $-3/2$, while that in the soft band is consistent with the results by *ROSAT*. At these flux limits, 30(± 3)% of the CXB in the 0.7–7 keV band and 23(± 3)% in the 2–10 keV band have been resolved into discrete sources. The average spectrum of faint sources detected in the total band shows a photon index of 1.63 ± 0.07 in the 0.7–10 keV range, consistent with the comparison of source counts between the hard and the soft energy band. Those detected in the hard band show a photon index of 1.49 ± 0.10 in the 2–10 keV range. These spectral properties suggest that contribution of sources with hard energy spectra become significant at a flux of 10^{-13} erg s⁻¹ cm⁻² (2–10 keV). The most plausible candidates are type-II AGNs, as indicated by on-going optical identifications.

Subject headings: cosmology: diffuse radiation — galaxies: active

1. Introduction

Since the discovery of the Cosmic X-ray Background (CXB) more than 35 years ago (Giacconi *et al.* 1962), its origin has been a key issue of the X-ray astronomy (for reviews see Fabian and Barcons 1992; Hasinger 1996). Although the emission extends over a wide energy range in more than 5 decades from X-rays to γ -rays, the main energy flux of the CXB is emitted in the hard X-ray band, peaked at ~ 20 keV. The spectrum resembles that of a hot plasma with a temperature of 40 keV (Marshall *et al.* 1980; Rothschild *et al.* 1983), and this introduced the possibility that hot plasmas uniformly fill the universe. However, little distortion of the Cosmic Microwave Background (CMB) spectrum by the Compton up-scattering measured with *COBE* ruled out this possibility, implying that the origin of the CXB is the superposition of faint discrete sources (Mather *et al.* 1994).

The understanding of the CXB origin has been quite different for the soft (< 2 – 3 keV), and the hard (> 2 – 3 keV) energy bands, respectively. In the soft X-ray band, the *ROSAT* satellite resolved 70% of the CXB in the 0.5–2 keV band into individual sources (Hasinger *et al.* 1998). Most of them are optically identified as (type-I) AGNs such as quasars (Schmidt *et al.* 1998). The average spectrum of these AGNs coincides with that of the CXB in the 1–2 keV range having a photon index of Γ of $\simeq 2$. The slope is steeper than that of the CXB extrapolated from above 2 keV, $\Gamma \simeq 1.4$ (e.g., Gendreau *et al.* 1995; Ishisaki *et al.* 1999).

By contrast, in the hard X-ray band above 2 keV, the origin of the CXB has been less well understood, due to lack of imaging instruments. *Uhuru* (Forman *et al.* 1978), *Ariel V* (McHardy *et al.* 1981), *HEAO1* (Piccinotti *et al.* 1982), and *Ginga* (Kondo *et al.* 1991) performed X-ray surveys above the 2 keV band. However, since they carried collimated-type detectors where the source confusion becomes significant, the achieved sensitivity limits are at most $\sim 10^{-11}$ erg $\text{s}^{-1} \text{cm}^{-2}$ (2–10 keV), and the sources observed by them only account for 3% of the total emission of the CXB in the 2–10 keV band. Moreover, for the hard X-ray background, there is a problem called the spectral paradox: bright AGNs observed with *HEAO1*, *EXOSAT* and *Ginga* have spectra with an average photon index Γ of 1.7–1.9 (e.g., Turner and Pounds 1989; Williams *et al.* 1992), which is significantly softer than that of the CXB itself, and hence, cannot be responsi-

ble for the total CXB emission. The spectra of these bright AGNs are consistent with the spectrum of the CXB fluctuation observed with *Ginga*, which shows $\Gamma = 1.8 \pm 0.1$ in the 2–10 keV range (Hayashida, Inoue, & Kii 1990; Butcher *et al.* 1997). Besides the spectral paradox, a discrepancy of source counts between the soft and hard energy bands has been noticed (e.g., Fabian & Barcons 1992). The normalization of the Log N - Log S relation in the 2–10 keV band obtained by the fluctuation analysis with *HEAO1* (Shafer and Fabian 1983) and *Ginga* (Butcher *et al.* 1997) is about 2 times larger than that obtained with the *Einstein* Medium Sensitivity Survey (MSS) in the 0.3–3.5 keV band (Gioia *et al.* 1984; 1990), if we convert the flux assuming a photon index of 1.7.

In order to study the nature of the X-ray source population over the 0.7–10 keV band, and to solve these unresolved problems on the CXB origin, we performed an unbiased imaging sky survey with the *ASCA* satellite (Large Sky Survey: LSS; Ueda 1996; Inoue *et al.* 1996). *ASCA* (Tanaka, Inoue, & Holt 1994), carrying four identical X-Ray Telescopes (XRT; Serlemitsos *et al.* 1995) coupled to two Solid-state Imaging Spectrometers (SIS; Burke *et al.* 1991; Yamashita *et al.* 1997), and two Gas Imaging Spectrometers (GIS; Ohashi *et al.* 1996; Makishima *et al.* 1996) as focal plane detectors, is the first imaging satellite capable of study of the X-ray band above 2 keV with a sensitivity up to several 10^{-14} erg $\text{s}^{-1} \text{cm}^{-2}$ (2–10 keV). It also covers the wide energy band from 0.5 to 10 keV, which allows us to directly compare results of the energy bands below and above 2 keV with single detectors, hence accompanied with much less uncertainties than previous studies. The first results from the LSS focusing on the 2–10 keV band data are reported by Ueda *et al.* (1998).

In this paper, we present the details of the analysis and the results, derived utilizing the whole data over the 0.7–10 keV band. In section 2, we summarize observations and data reduction. In section 3, we describe analysis methods and results. A complete X-ray source list in the LSS field is presented. In section 4, we evaluate possible systematic errors in our results, based on studies by Monte Carlo simulations. In section 5, Log N - Log S relations are derived in three survey bands (0.7–7 keV, 2–10 keV and 0.7–2 keV). In section 6, we discuss implication of the results.

2. Observations and Data Reductions

2.1. Observations

The survey field of the LSS is a continuous region near the north Galactic pole, centered at $RA(2000) = 13^h14^m$, $DEC(2000)=31^\circ30'$. We had no bias in selecting this field except that we avoided bright X-ray sources with a flux greater than $\sim 10^{-11}$ erg s $^{-1}$ cm $^{-2}$ (2–10 keV) in the major X-ray source catalogs in order to minimize complexity in the analysis that would be induced by bright sources. The Galactic neutral hydrogen column density toward the LSS field is $N_H = 1.1 \times 10^{20}$ cm $^{-2}$, which is sufficiently low to study extra-Galactic sources above 0.7 keV.

The observation log of the LSS is summarized in Table 1. Seventy-six pointings have been made in total (16 pointings in Dec. 1993 and Jan. 1994, 20 pointings in June 1994, 20 pointings in Dec. 1994 and Jan. 1995, and 20 pointings in June/July 1995) with a typical exposure of 10 ksec per pointing. Shifting the pointing positions by the half size of the SIS FOV in sequence, we observed each sky point twice with the SIS so that the sum of field of views (FOVs) of the SIS ($22' \times 22'$) covered the survey area continuously with good overlaps. This operation makes the sensitivity limits quite uniform over the entire field. The total sky area observed with the GIS and SIS amounts to 7.0 deg 2 , and 5.4 deg 2 , respectively. The mean exposure time per point is 56 ksec (sum of GIS2 and GIS3), and 23 ksec (sum of SIS0 and SIS1) after data screening.

2.2. Data Reduction

Since the LSS observations consist of many pointings, we created images in the sky coordinate system (Gotthelf 1996) to be superposed in a common coordinate to all the data. Photons were accumulated in the different energy bands of 0.7–7 keV, 2–7 keV, and 0.7–2 keV for the SIS, and 0.7–7 keV, 2–10 keV, 0.7–7 keV, 2–4 keV, and 4–10 keV for the GIS so that we can get the spectral information from energy-dependent image analysis. We did not use energies below 0.7 keV, nor energies above 10 keV (7 keV for the SIS), because the contamination by the Non X-ray Background (NXB) is high relative to X-ray events (e.g., Kubo *et al.* 1994). We utilized as much data as possible, so that the Signal to Noise (S/N) ratio should be optimized for faint source detection (Ueda 1996). We discarded data of the outer part of the GIS images

with a radius larger than 17 arcmin from the optical axis, which are not suitable for study of faint sources because (1) the NXB rate is high (Kubo *et al.* 1994), (2) those data are greatly affected by the stray light from the CXB outside the FOV (Ishisaki 1996), and (3) the Point Spread Function (PSF) of the XRT have not been directly measured through the observations of Cyg X-1 (Takahashi *et al.* 1995).

The nominal error of the attitude solution of *ASCA* is about 1 arcmin (Gotthelf 1995), and arises from the mis-alignment between the focal plane detectors and attitudes sensors (Ueda *et al.* 1999). The error depends on the temperature of the satellite baseplate. In our analysis we corrected for this error when converting from the detector coordinate to the sky coordinate, using the onboard house-keeping data according to the method described in Ueda *et al.* (1999). This reduces the systematic positional error, due to the absolute attitude error, to 0.5 arcmin in radius (90% confidence level). Consequently, we could greatly improve the quality of images superposed from the multi pointings with different orbit conditions of the satellite. The final position uncertainties, which contain statistical errors, are evaluated in the next section.

3. Analysis and Results

Extremely careful analysis is required to study faint sources with *ASCA*. First, the PSF of the XRT has a large scattering tail, which affects flux determination of a faint source near a brighter one. The PSF itself strongly depends on the position of the detector as well as photon energy (Serlemitsos *et al.* 1995). The background, consisting of the CXB and the NXB, also depends on the position and energy. It should be noted that the intensity of the NXB can fluctuate by a factor of 10–20% from pointing to pointing (Ishisaki *et al.* 1997). Furthermore, there is a grid support on the GIS detector (Ohashi *et al.* 1996), which should be taken into account in calculating fluxes of sources falling near its structure. Under these conditions, we must pay attention so that real sources are found completely but statistical fluctuations are not picked up. Also, we should be very careful in determining fluxes of faint sources, which are highly sensitive to background subtraction under the low S/N ratio.

To overcome these difficulties in analysis of *ASCA* data, we developed a new source-detection method (Ishisaki *et al.* 1995; Ueda 1996; Takahashi *et al.*

1998). In this procedure we take fully account of the complicated detector responses, such as the position-dependent PSF, the background, the vignetting of the XRT, and the grid shadows of the GIS. The procedure consists of two steps: (Step I) detection of source candidates and (Step II) calculation of their statistical significances and fluxes. A source candidate whose significance exceeds a certain threshold is regarded as a detected source. In each step we treat data of the GIS and the SIS separately. Finally, their results are combined to improve statistics.

3.1. Step I: Source Detection

In Step I, we smooth the raw image (= the image in the sky coordinate in the photon counts space) in order to effectively detect even faint sources. However, a simple convolution of the image data with an axisymmetric, position-independent smoothing kernel would not be sufficient, because the PSF depends strongly on the position of the source in the focal plane of the XRT. Noticeably, the PSF elongates toward the azimuthal direction and squeezed in the radial direction if the point source is off the optical axis of the XRT (e.g., Takahashi *et al.* 1994). We therefore smooth the images by cross correlating with position-dependent PSFs in detector coordinates, which are converted from the sky coordinates with information from the satellite attitude. The cross correlation function (CCF) is calculated as:

$$F(\vec{x}) = \int d\vec{x}' F_0(\vec{x}') P(\vec{x} : \vec{x}'),$$

where \vec{x} represents positional coordinate, $F_0(\vec{x})$ is the raw image, and $P(\vec{x} : \vec{x}')$ is the PSF intensity at \vec{x}' with peak at \vec{x} . In calculating the CCF, proper modeling of the PSF is very important. For the GIS, we adopted a synthetic PSF modeled as a two dimensional gaussian squeezed in the radial direction as a function of the offset angle (Ishisaki *et al.* 1995). For the SIS, we used the ray-tracing program (Tsusaka *et al.* 1995) to reproduce the PSF at any position in the focal plane.

Since the brightness profile of the background (CXB + NXB) peaks around the optical axis and decreased to about 50% at the edge of the GIS FOV (Kubo *et al.* 1994; Ueda 1996), it becomes harder to detect sources located at larger radii. Hence, we subtract the background from the raw image before smoothing the GIS image. The background model is produced by the superposition of 109 pointings onto blank skies

whose total exposure amounts to about 1 Msec. On the other hand, we neglect this process for SIS data because the position dependence of the background is much smaller due to its narrower FOV.

After smoothing the raw images separately for each sensor and pointing, we superpose all the smoothed images into a single image with a larger size. Finally, we correct it for the exposure by dividing with a superposed exposure map that are smoothed in the same way. Figure 1 shows a contour map of the GIS image in the 0.7–7 keV band thus created.

Next, we perform detection of source candidates from the smoothed (and exposure-corrected) image created above. Since a point source appear as a cluster of pixels having high counting rates in the smoothed image, source candidates are picked up if the highest pixel in the cluster exceeds some threshold level. The level is varied from a high to a low level continuously and a newly appeared cluster is added to the source-candidate list. This makes it possible to find all faint sources completely even when brighter sources are located around them. The list of the identified clusters is used as inputs for the fitting process in Step II. The position of the highest pixel in each cluster gives the source position.

3.2. Step II: Flux Calculation

In Step II we evaluate the statistical significances of the candidate sources, and calculate their fluxes. The analysis is performed using two-dimensional fitting to the raw image in the photon count space, superposed from the multi pointings. An advantage of this method is that we can determine the local background level from the observed image itself, which is otherwise difficult to estimate with enough accuracy to determine correct fluxes of faint sources. We apply various corrections, such as exposure and vignetting, to the model function, not to the data.

The fitting model is basically a sum of the background image, and the PSFs at the location of the source candidates. To reproduce the superposed sky image in the model calculation, we sum up contributions of PSF and background from different pointings weighted with exposures. The intensities of the sources and the background are free parameters to be determined through the fitting. The source positions are fixed to the values determined from the smoothed image in Step I. Due to the vignetting of the XRT, an observed count rate from a source with a given flux

decreases as the offset angle from the optical axis becomes larger (Serlemitsos *et al.* 1995). To derive an intensity of a source, we correct for this effect in the model calculation, so that we should obtain the count rate when the source is observed at a reference position in the focal plane. The reference position is taken to be a 8.5 arcmin (7 arcmin for the SIS) off axis position, and the count rate is defined as that integrated within a radius of 6.0 mm (corresponding to about 5.9 arcmin) for the GIS and 4.0 mm (about 3.9 arcmin) for the SIS. These vignetting correction factors are calculated from the XRT response, which is well calibrated using the Crab observations, as described in Appendix A. For the GIS, source peaks are modeled by the real PSFs obtained from the Cyg X-1 observations (Takahashi *et al.* 1995; Ikebe *et al.* 1997), and the background is from the same model, as used in Step I (superposition of real images of blank skies). For the SIS, the PSF and the CXB are reproduced by the ray-tracing program, and the NXB is modeled using the night-Earth data (Ueda 1996). The systematic errors in the PSF models are estimated to be 5% and 15% for the GIS (Takahashi *et al.* 1995), and the SIS (Kunieda *et al.* 1995), respectively, and are taken into account in the fitting process. Finally, the transmission map of the grid support is multiplied to the component of sources (PSFs) for the model of the GIS. Since the shape of the PSF and the vignetting correction factor depend also on energy, we need to assume a spectrum of a source in the model calculation. We adopted a power law with a photon index of 1.7 as a typical spectrum. The dependences of the PSF and the vignetting correction factor on the assumed spectrum are negligible within a reasonable region of the photon index (the difference of the vignetting correction factor between $\Gamma = 1.0 - 2.0$ is less than a few percent).

Since the number of photons in one bin of the image is small, we use Poisson maximum likelihood statistics to find the best fit parameters. The maximum likelihood function is defined as:

$$\text{Likelihood} = \sum_{i,j} \{-m(i,j) + d(i,j) \times \log m(i,j)\},$$

where (i,j) represents the position of the bin, m is the model, and d is the data. The sum is taken over the region used in the fitting. In this statistics, 1σ statistical error of one parameter is defined as a deviation from the best fit value, when the Likelihood decreased by 0.5 from its maximum. The

significance of detection is defined as (best fit flux)/(1σ statistical error of the flux).

For the fitting to converge correctly, the free parameters, namely normalization of background and those of peaks, are determined one by one in the fitting process. We first fit the image only with the background component (CXB + NXB) to determine the background level. Next, taking the background determined in this way, we determine the flux of the brightest source. After the flux is obtained, this is then frozen and the process is repeated for the next source. Once all the detected source candidates are fitted, the parameters including the normalization of background are allowed to float, producing final parameters. Thus, any statistical coupling between the free parameters are taken into account. In the procedure, we do not treat all fields of the LSS simultaneously. Instead, we divided the entire image into small regions ($19' \times 19'$ for the GIS and $14' \times 14'$ for the SIS) so that the number of sources becomes appropriate (<29) for one fitting process. To take into account the PSF tails from sources in outer region of the selected area, we fit the image of larger size with some margins ($6'$ for the GIS, and $4'$ for the SIS) when determining the flux of sources within the selected area. We did not use data of a rectangular region surrounded by four corners, $(RA(2000), DEC(2000)) = (13^h19^m5^s, 33^\circ6')$, $(13^h20^m15^s, 32^\circ58')$, $(13^h21^m3^s, 33^\circ15')$, and $(13^h19^m52^s, 33^\circ23')$, to avoid systematic errors due to a bright extended source located there.

3.3. The Source List

First, we applied the methods described above to the combined image of the LSS field separately for the GIS and the SIS in three energy bands: the total band (0.7–7 keV), the hard band (2–10 keV; 2–7 keV for SIS), and the soft band (0.7–2 keV). We thus obtained 6 preliminary source lists. At this stage we adopted relatively loose detection criteria (above 3.2σ) in selecting sources. We then merged the three source lists in different bands to one list for each detector. Due to statistical fluctuation, the detected positions of a source can differ with energy bands. Here, we regarded any pair of sources detected in different energy bands as identical, if their positions coincide within 1.5 arcmin (1 arcmin for the SIS). These criteria are reasonable, considering the position accuracy of each detector. We adopted a position determined in an energy band where the maximum significance was obtained. Finally, we combined the GIS list and

the SIS list, regarding sources detected with different detectors within a distance of 1.5 arcmin as identical sources. We adopted the positions determined by the SIS data, taking advantage of its superior positional resolution (hence better position accuracy), except for those located out of the combined SIS FOVs. Because the PSF of the XRT measured with the SIS has a sharp core, we can resolve neighboring sources whose angular separation is as small as 1 arcmin.

Using the combined source list as inputs of source candidates, we repeated Step II in each energy band. Finally, we adopted the following criteria for detection: (1) the significance of summed count rate of the GIS and the SIS (σ_t) should exceed 4.5, and (2) the significance of either the GIS or the SIS (σ_g or σ_s) should also exceed 3.5. Studies based on Monte Carlo simulations justify the validity of setting these criteria, as described below. Using σ_t , the combination of two significances measured with independent detectors, considerably reduces contamination by fake sources (statistical fluctuation), since real sources are expected to be commonly detected with both the GIS and the SIS, while fake sources are not.

With these criteria, we detected 105, 44, and 72 sources, in the total, the hard, and the soft energy bands, respectively. The total number of sources is 107. The number of sources detected both in two energy bands (or only in one band) is summarized in Table 2. Table 3 gives the complete source list in the LSS field with their positions, significances, and vignetting-corrected count rates in the three energy bands. Note that the GIS count rate of 1 c ksec⁻¹ in each energy band corresponds to a flux of 6.4×10^{-14} (0.7–7 keV), 1.1×10^{-13} (2–10 keV), 4.5×10^{-14} (0.7–2 keV) erg s⁻¹ cm⁻², respectively, for a power-law spectrum with a photon index of 1.7. All the fluxes in this paper are corrected for the Galactic absorption ($N_H = 1.1 \times 10^{20}$ cm⁻²) to give unabsorbed fluxes. In Table 4, we list the conversion factors from the count rate to flux for several photon indices assumed.

3.4. Spectra of the Detected Sources

Spectral properties of these faint sources are of particular interest in discussing the origin of the CXB. The count rates of the hard and the soft bands already contain information of the spectrum for each source. To derive more information, particularly spectra within the 2–10 keV range, we repeated the image fitting procedure (Step II) in finer energy bands (2–4 keV and 4–10 keV) for the GIS data. Then, we

produced spectra for each source in two energy bands for the SIS (0.7–2 and 2–7 keV), and in three energy bands (0.7–2, 2–4, and 4–10 keV) for the GIS. For each source, we fitted the GIS and the SIS spectra simultaneously, assuming a power law with an absorption fixed at the Galactic column density of $N_H = 1.1 \times 10^{20}$ cm⁻². In the spectral fitting, we used an Auxiliary Response Function (ARF), constructed for a point source located at the reference position defined above, where the obtained count rate is normalized. The best-fit power law indices obtained are given in a column of Table 3, with 1σ statistical errors. Figure 2 shows a correlation between a flux and a photon index determined in the 0.7–10 keV range. In the figure, the flux (0.7–7 keV) is converted from the GIS count rate in the 0.7–7 keV band, assuming a photon index of 1.6 (an average index for a faint source sample; see below).

In order to see the statistical properties of these sources, we next made average spectra of sources for the three survey bands (the total, hard, and soft band) by summing up the spectrum of individual sources. Since this operation corresponds to calculating a flux-weighted average, very bright sources dominate the signal and significantly affect the result. To study the property of faint sources, we therefore use flux-limited samples for each survey band: sources with fluxes (in units of erg s⁻¹ cm⁻²) of $0.5 - 2.0 \times 10^{-13}$ (0.7–7 keV) detected in the total band, those with fluxes of $0.8 - 4.0 \times 10^{-13}$ (2–10 keV) detected in the hard band, and those with fluxes of $0.3 - 3.0 \times 10^{-13}$ (0.7–2 keV) detected in the soft band. We hereafter refer to them as the total-band sample, the hard-band sample, and the soft-band sample, each of which consists of 74, 36, and 64 sources, respectively.

We fitted these average spectra with a power law with the Galactic absorption. Since the SIS spectra do not cover the energy band above 7 keV, we here use only the GIS spectrum to make the statistical weight uniform over the entire 0.7–10 keV range. The spectral fit is performed in two energy ranges: 0.7–10 keV band consisting of three bins (0.7–2, 2–4, and 4–10 keV) and 2–10 keV band consisting of two bins (2–4 and 4–10 keV). The fitting results are summarized in Table 5. We obtained an average photon index of 1.63 ± 0.07 (1σ statistical error) in the 0.7–10 keV range for the total-band sample. The 2–10 keV photon indices are 1.63 ± 0.18 , 1.49 ± 0.10 , and 1.85 ± 0.22 for the total, the hard, and the soft band sample,

respectively (the 2–10 keV index of the hard band sample is not exactly same as the value reported in Ueda *et al.* (1998) because of inclusion of σ_s in the detection criteria).

It should be noted that the average spectrum in the 0.7–10 keV band for the hard-band sample (or the soft-band sample) is subject to a statistical bias in the sense that average spectrum of the hard- (soft-) band sample tends to show a harder (softer) spectrum than in reality: if sources are selected based on significances only in the hard (soft) band, there should be a sampling effect that a sample selectively contains sources whose “observed” spectra in the 0.7–10 keV band are hard (soft) merely due to statistical fluctuation. Hence, the two values in parenthesis in Table 5 should not be considered to reflect a real property, without correcting for these biases. On the other hand, no such bias exists, when we discuss a spectral property in the 2–10 keV range for all the samples.

4. Verification

4.1. Flux Uncertainty

Here we evaluate systematic errors in the obtained fluxes and spectra. In general, systematic errors can be divided into two categories. In the first category are errors caused by the calibration uncertainty. Appendix A evaluates this error in detail. The uncertainty in the absolute photometry of *ASCA* is conservatively estimated at 10%. The error in the relative flux is estimated to be 8% for an individual source, and is much smaller for an average of many sources. Note that this error is smaller than the statistical error for a faint source detected with a significance less than 12σ ($1/12 \sim 8\%$). In the second category are errors associated with the improper analysis method or those inevitably caused by principles (such as the source confusion), which remain, even if we fully understand the response functions of instruments.

To begin with, we compared the fluxes obtained from the GIS and the SIS to check the consistency within our data. We have 71 sources detected with both the GIS and the SIS above 3.5σ (and $\sigma_t > 4.5$) in the total band. Figure 3 shows a comparison in the form of a scatter-plot between the fluxes obtained with the SIS and the GIS for this sample. Since the spectrum of an individual source at faint flux levels includes a large statistical error, we assumed a photon index of 1.6 for all sources to convert a count rate to a flux. As shown in the figure, we found a good

correlation between the GIS and the SIS fluxes.

Studies by Monte Carlo simulation are indispensable to check systematic errors of the second category, which are otherwise difficult to evaluate. We developed an instrument simulator that simulates the response of *ASCA* (Hirayama *et al.* in preparation; an example of analysis utilizing it is given in Ikebe *et al.* 1997). The complicated responses of the instruments, in terms of PSF, vignetting, grid shadow of the GIS, etc, are taken into account in the simulator. The simulator produces a photon list from the input sky image and spectrum, according to the probability distribution in the responses, which are well calibrated (Appendix A).

To simulate the LSS data, we generated photon lists with the same conditions (such as exposure and satellite attitude) as the LSS observations. Sky images were created according to the Log N - Log S relation obtained by Ueda *et al.* (1998), assuming that it extends towards a lower flux level with a function of $N(> S) \propto S^{-3/2}$, until the whole intensity of the CXB is explained by integral of sources. For simplicity, all the sources are assumed to have a single spectrum regardless of the flux level: a power law with a photon index of 1.7 over the full energy range (0.7–10 keV). The NXB was added based on the night Earth data, and we fluctuated its intensity from pointing to pointing by a factor of 10%, considering the uncertainties in the modeling of the NXB (Ishisaki *et al.* 1997). We then analyzed the simulated data obtained in this way, and applied our source finding procedure in exactly the same manner as for the real data. To reduce the statistical fluctuation in the simulated result, we ran the simulations several times, with a corresponding exposure of 23 Msec in total.

Figure 4(a) shows a comparison of the calculated flux with the input flux for these simulated data. Here, we define the input flux as the flux of the brightest source within a 1 arcmin radius around the detected position, considering the angular resolution of the PSF. As noticed from the figure, we obtain a good agreement between input and output flux in general, although there is a tendency for the observed fluxes to become larger than the input ones, when the flux is below $\sim 2 \times 10^{-13} \text{ erg s}^{-1} \text{ cm}^{-2}$ (0.7–7 keV). This can be attributed to two effects. One is the bias due to the statistical fluctuation of photon numbers: we selectively detect sources whose output fluxes are larger than the input fluxes around the sensitivity limit, because the significance is determined by an output flux

(i.e., observed count rate) rather than by an input flux. The second effect is the source confusion by nearby sources: the observed flux contains all the integrated flux from sources that cannot be resolved around the detected position.

Figure 4(b) shows a histogram of the ratio of the input flux to the output flux. In the same figure, we also show a similar histogram, marked with a dashed line, for the case when we define the input flux as an integrated (not the brightest) flux within a radius of 1 arcmin around the detected position. As expected, the ratio (input/output) becomes systematically larger for the latter definition. The difference of the mean value between these two histograms quantitatively gives the effect of the source confusion. We thus estimate the contamination by nearby sources in the observed flux to be about 10% on average. This means that effects due to the source confusion are not serious in our analysis, since the number density of the detected sources, derived below ($\sim 10\text{--}20\text{ deg}^{-2}$), is small enough compared with the confusion limit determined by the beam size ($\sim 1\text{ arcmin}$).

From Figure 4, it can be seen that there are several sources detected with an extremely high flux, relative to the input flux. These are considered to be not real sources but “fake” sources, produced by the statistical fluctuation of the background. We estimate the fraction of fake sources to be at most a few percent in the overall detections. In other words, the probability to pick up a fake source by our source finding method is about $\sim 0.5\text{ deg}^{-2}$ with the detection criteria we adopted in this paper (4.5σ).

We also check the accuracy of the output spectra. From a scatter plot between a photon index and a flux obtained for the simulated data, we confirmed that the output photon index scatter around the input value (1.7) and there is no significant systematic change with respect to the flux level. We also verified that the summed spectra for the flux-limited samples, defined above, are consistent with the input spectrum within a statistical error. These results confirm the validity of the spectrum determination by our analysis method.

4.2. Position Accuracy

The source position in the source list contains (i) an error arising from the uncertainty of the absolute attitude solution, (ii) a statistical error due to limited number of photons, and (iii) a systematic error

caused by source confusion. As described earlier, the first term is evaluated to be 0.5 arcmin in radius (90% confidence level). To evaluate the combined error of the remaining two, we again analyze the simulated data. Figure 4(c) shows a histogram of angular distance between the detected position, and the position of the brightest source within a 1 arcmin radius, which should be taken as a real counterpart. According to this histogram, the error comes out to be 0.6 arcmin (90% confidence level). When limiting for sources that are detected also in the hard (or the soft) band with significances above 4.5σ , we found the error reduces to 0.4 arcmin. Hence, taking a root sum square of all possible errors, we estimate the final positional error to be 0.6–0.8 arcmin in radius (90%), depending on the detection significance. To improve it further, observations with the *ROSAT* HRI are ongoing.

5. The Log N - Log S Relation

5.1. Relation of Observed Area and Sensitivity

The Log N - Log S relation (number-flux relation; $N(S)$ in the differential form and $N(> S)$ in the integral form) is the most fundamental measure which directly describes the contribution of individual sources to the CXB. To derive the Log N - Log S relation, it is necessary to calculate the survey area, Ω , as a function of flux S , or in other words, to determine the sensitivity limits over the entire survey field. The sensitivity limits depend on parameters such as exposure, effective area (vignetting), the background level, and the shape of the PSF. It is not an easy task, however, to compute it by an analytic formula due to the following reasons: (1) the image is composed of multiple pointings, and the above parameters are different from position to position. (2) Our source-finding method is based on image fitting, and thus the estimates of the sensitivity limits are not trivial.

To estimate the detection significance for a given flux at any position in the survey field, we utilized the model function used in the source finding procedure. We first compute an image model around the source position, which consists of a point source with the given flux and the background. Then we fit the computed image with the same model function, varying the flux of the source as a free parameter. Using the same principle in the fitting process given in Section 3.2, we can derive the statistical error of

the flux, thus the significance of detection, expected for the given flux. We confirmed the validity of this method by comparing the result with a more realistic simulation, in which the number of photons fluctuates according to Poissonian statistics. This procedure is repeated for several different fluxes, as to determine the sensitivity limits over the entire field for given detection criteria, which thus enables us to compute $\Omega(S)$. In practice, we define S as a count rate (corrected for the vignetting) rather than as a flux, because the detection significance is simply extracted from a count rate.

We compute $\Omega(S)$ separately for the GIS and the SIS, because the ratio of count rates between the GIS and the SIS depends on the source spectrum, which makes it difficult to combine the two results. Thus, when deriving $\Omega(S)$, and hence the Log N - Log S relation, we adopted the following detection criteria applied separately to the GIS or the SIS: (1) $\sigma_g > 3.5$ ($\sigma_s > 3.5$ for the SIS), and (2) $\sigma_t > 3.5$. Note that the criteria are different from those adopted in making the source list (Section 3.3). The second condition is added just to reduce the fraction of fake sources. Figure 5(a) shows results for $\Omega(S)$ computed for the three survey bands. The GIS achieves higher sensitivity than the SIS in the hard band, while the SIS achieves higher sensitivities in the total and the soft bands, as is expected from the energy dependence of their detection efficiencies. The number of sources detected with the same detection criteria per unit logarithmic flux range are plotted in Figure 5(b). Dividing these numbers by $\Omega(S)$, we can derive “observed” Log N - Log S relation, $N(S)$, in the differential form. In plotting Figure 5, we converted the count rate to flux assuming a photon index of 1.6 (0.7–7 keV), 1.5 (2–10 keV), and 1.9 (0.7–2 keV).

5.2. Biases on the Observed Log N - Log S Relations

The “observed” Log N - Log S relations are, however, considered to be subject to some biases. They include (1) bias induced by the statistical fluctuation of the measured flux (Eddington’s bias), (2) effect of the source confusion, (3) inefficiency of the source detection, and (4) contamination by fake sources. Again, Monte Carlo simulations are the most powerful mean to estimate these biases. Using the set of simulated data created in Section 4, we calculated $\Omega(S)$ and derived the Log N - Log S relation in the same manner as for the real data.

Figure 6 show the results of integral Log N - Log S relations derived from the simulated data. The faintest points in the total and the soft band are determined mainly by the SIS, while those in the hard band are determined by the GIS. The input Log N - Log S relation is plotted by a dashed line in the same figure. As noticed, the results of the simulation are almost consistent with the input parameters, although week systematic deviations can be found. The points near the sensitivity limit in the total and soft band determined by the SIS data are located slightly above the input line by 10–20%. In the soft band, the GIS result are also $\sim 10\%$ above the input at the flux level below $\sim 10^{-13}$ erg s $^{-1}$ cm $^{-2}$ (0.7–2 keV). The reason why this deviation is seen only in the soft band can be explained in terms of the source confusion, since the positional resolution of the GIS becomes worse for lower energy (Ohashi *et al.* 1996) and the effect should be most significant in the soft energy band.

5.3. The Integral Log N - Log S Relations

Finally, we derived Log N - Log S relations from the real data correcting for these biases. From the simulation, we found an empirical formula can be applied to correct them, by scaling the “observed” integral Log N - Log S relation, $N(> S)$, by a flux-dependent factor, f , which is defined as:

$$\begin{aligned} \text{(For } N > N_0) \quad f &= 1/[0.1 \times (\log N - \log N_0)/(\log N_1 - \log N_0) + 1] \\ \text{(For } N < N_0) \quad f &= 1, \end{aligned}$$

where N is the observed integral source counts in units of deg $^{-2}$. The scaling factor becomes 10% at the source number density of $N = N_1$, and 0% at $N < N_0$. We set $N_0 = 15$ deg $^{-2}$ and $N_1 = 30$ deg $^{-2}$ for the SIS results for any band, and $N_0 = 3$ deg $^{-2}$ and $N_1 = 15$ deg $^{-2}$ for the GIS results only in the soft band. No correction is applied for the GIS results in the other bands since no significant biases were seen in the simulation. Note that this formula can be applied only in the currently interesting number-density range ($N \lesssim N_1$).

Figure 7 shows the final results of integral Log N - Log S relations in the three survey bands after applying this formula. Here, we convert the count rate in each band into the flux in the same energy band, assuming a photon index of 1.6 (0.7–7 keV band), 1.5 (2–10 keV band), and 1.9 (0.7–2 keV), each of which corresponds to a photon index of the average spectrum of the faint-source sample, as defined in Section 3.4. The 90% statistical errors in the source number counts are plotted at several data points.

6. Discussion

6.1. The Log N - Log S Relation

From the LSS, we determined the Log N - Log S relation by direct source counts in the three survey bands, 0.7–7 keV, 2–10 keV, and 0.7–2 keV. These results were obtained by the careful analysis based on extensive instrumental calibration and detailed simulation studies. In the 0.7–7 keV band, where the sensitivity is optimized for most of sources except for very soft or hard sources, we found that the Log N - Log S relation is well represented with $N(> S) \propto S^{-3/2}$ over a wide flux range from 7×10^{-14} to 8×10^{-13} erg s $^{-1}$ cm $^{-2}$ (0.7–7 keV). As already reported in Ueda *et al.* (1998), the 2–10 keV Log N - Log S relation lies on the extrapolation from the previous results by *HEAO1 A2* (Piccinotti *et al.* 1982) and *Ginga* (Kondo *et al.* 1990) with a euclidean slope of $-3/2$. The result is consistent with the fluctuation analysis by *ASCA* (Gendreau, Barcons, & Fabian 1998).

To compare our results in the 0.7–2 keV band with previous studies, we superpose the Log N - Log S relation obtained by *ROSAT* (Hasinger 1998) in Figure 3 (c). Here we convert the flux from 0.5–2 keV to 0.7–2 keV assuming a photon index of 1.9. As shown in the figure, our results are consistent with the *ROSAT* results (and also with *Einstein* results; see Primi *et al.* 1991) within statistical error, although we find a discrepancy that the *ASCA* source counts is slightly higher by 20 ~ 30%.

There could be two explanations for this discrepancy. One is due to the calibration uncertainty in the flux (Appendix A). In addition to the uncertainty of the absolute photometry ($\sim 10\%$), the low energy response of the *ASCA* has an uncertainty of $\sim 3 \times 10^{20}$ cm $^{-2}$ in a neutral hydrogen column density, which could produce an error of $\sim 5\%$ in the 0.7–2 keV flux. Note that a systematic error of 10% in the flux leads to $\sim 15\%$ apparent difference in the source counts. The other explanation could be attributed to the nature of the detected sources. Even though *ASCA* and *ROSAT* cover the common energy band of 0.7–2 keV, the “effective” band at which detection efficiency is maximized is different: the *ASCA* GIS/SIS has better detection efficiency toward higher energy in the 0.7–2 keV range (e.g., Ohashi *et al.* 1996), while the *ROSAT* PSPC has a peak efficiency around 1 keV (Pfeffermann *et al.* 1986) and also covers the energy range below 0.7 keV. If some fraction of sources has hard energy spectra in the 0.7–2 keV

range (e.g., absorbed spectra), they are more easily detected with *ASCA* than *ROSAT*. For example, if half sources in the soft-band sample have absorbed spectra with $N_H = 3 \times 10^{21}$ cm $^{-2}$ with a photon index of 2.2 and the other sources are unabsorbed, discrepancy of $\sim 10\%$ in the source counts can be produced, if we simply take a photon index of 1.9 in the flux conversion between *ROSAT* and *ASCA* assuming a single population.

6.2. The Resolved Fraction of the CXB

The resolved fraction of the CXB depends on the absolute intensity of the CXB emission, which can be different by about 20% in the literature (e.g., Marshall *et al.* 1980; Gendreau *et al.* 1995; Ishisaki *et al.* 1999). To eliminate uncertainty in the absolute photometry of instruments and the field-to-field fluctuation of the surface brightness of the CXB, we adopt the result by Ishisaki *et al.* (1999) that are obtained with the same instrument (GIS) from the same field (LSS). Correcting for the contribution of brighter sources than the brightest sources in the LSS field, we use $(7.0 \pm 0.7) \times 10^{-8}$ erg s $^{-1}$ cm $^{-2}$ Str $^{-1}$ (0.7–7 keV) and $(6.5 \pm 0.7) \times 10^{-8}$ erg s $^{-1}$ cm $^{-2}$ Str $^{-1}$ (2–10 keV) as the whole CXB intensity. Note that this 2–10 keV flux is larger by 23% than the result by Marshall *et al.* (1980). The error (10%) shows the systematic error due to uncertainty of the evaluation of the stray light in the analysis of the CXB spectrum (Ishisaki *et al.* 1999). The Log N - Log S relations obtained in this paper indicate that 30(± 3)% of the CXB has been directly resolved into discrete sources with a sensitivity limit of 6×10^{-14} erg s $^{-1}$ cm $^{-2}$ in the 0.7–7 keV band, and 23(± 3)% with a sensitivity limit of 1×10^{-13} erg s $^{-1}$ cm $^{-2}$ in the 2–10 keV band. The attached error merely comes from the uncertainty of the CXB intensity described above.

6.3. Comparison of Log N - Log S Relations in the Soft and the Hard Band

The comparison of Log N - Log S relations between soft and hard bands provides spectral information over the whole 0.7–10 keV energy band. Assuming a single population of sources, we can constrain the average spectrum of sources so that the hard and soft Log N - Log S relations should be consistent. Previously, this kind of comparison has been made, based on results of different satellites (such as *Ginga* and *Einstein*), which could be subject to uncertainty in the mutual calibration between different instruments.

Since *ASCA* covers the energy bands above and below 2 keV with single detectors, we can now discuss it with much less uncertainties than in previous studies. Figure 8 shows the Log N - Log S relation in the soft band (0.7–2 keV), superposed on the Log N - Log S relation in hard band (2–10 keV). The 0.7–2 keV count rate is converted to the 2–10 keV flux, assuming two power-law photon indices (1.4 and 1.7). As noticed from the figure, the two Log N - Log S relations coincide with each other if we choose a photon index 1.5–1.7 at a flux level of $(1 \sim 2) \times 10^{-13}$ erg s $^{-1}$ cm $^{-2}$ (2–10 keV). Indeed, the result is consistent with the average spectrum of the total-band sample, which shows a photon index of 1.63 ± 0.07 in the 0.7–10 keV range.

6.4. Spectral Properties of the Detected Sources

The most important result is finding evidence for the solution of the spectral paradox (Ueda *et al.* 1998). The average spectrum of the hard band sample, consisting of sources detected in the hard band with fluxes of $(0.8 - 4) \times 10^{-13}$ erg s $^{-1}$ cm $^{-2}$ (2–10 keV), shows a photon index of 1.49 ± 0.10 in the 2–10 keV range (1σ statistical error in the mean value). This is significantly harder than the spectrum of sources at much brighter flux level obtained by previous studies, such as the fluctuation analysis with *Ginga* that showed a photon index of 1.8 ± 0.1 (Butcher *et al.* 1997). Moreover, the photon index is very close to that of the CXB in the 2–10 keV range, $\Gamma \simeq 1.4$ (e.g., Gendreau *et al.* 1995; Ishisaki *et al.* 1999), to within statistical errors.

When the energy range is expanded to below 2 keV, the photon index in the 0.7–10 keV range for the total band sample, ~ 1.6 , also suggests a similar hardening of average spectrum of sources with decreasing flux. The spectrum of the CXB can be approximated with a power law of $\Gamma \simeq 1.5$ in the 0.7–10 keV range when the soft component below 1.2 keV is appropriately modeled (Gendreau *et al.* 1995; Ishisaki *et al.* 1999). Thus, even in the 0.7–10 keV range, the average spectrum of sources becomes close to the CXB spectrum.

These spectra of sources at a flux level of $\sim 10^{-13}$ erg s $^{-1}$ cm $^{-2}$ (2–10 keV) are harder than a typical spectrum of bright type-I AGN, both in the 2–10 keV and 0.7–10 keV range (e.g., Williams *et al.* 1992; Nandra & Pounds 1994; George *et al.* 1998). This implies that a population of sources with hard energy spectra that is responsible to the CXB emission begins to dominate in the sensitivity limits we achieved.

6.5. Populations in Our Sample

Using results from optical identifications in the *ROSAT* surveys, we can make a rough estimate of the fraction of well-known X-ray populations in our survey, such as type-I AGNs, clusters of galaxies (CG), and stars. In the 0.7–2 keV band, their fractions are expected to be same as the *ROSAT* survey. According to the results by *ROSAT* at a flux of $10^{-13} - 10^{-14}$ erg s $^{-1}$ cm $^{-2}$ (0.5–2 keV) (e.g., Hasinger 1996; Bower *et al.* 1996), about 60% of the total sources are identified as type-I AGNs and 10% are clusters of galaxies. The fraction of Galactic stars depends both on the flux limit and on the Galactic latitude. We estimate that 10–15% of the LSS sources detected in the soft band can be stars, considering the high Galactic latitude of the LSS field.

The other populations contain objects identified as narrow emission line galaxies (NELGs), and unidentified ones in the *ROSAT* surveys. Recently, however, Hasinger *et al.* (1998) and Schmidt *et al.* (1998) pointed out that a part of the previous identifications with NELG using the Position Sensitive Proportional Counter (PSPC) could be incorrect because of a large position uncertainty and the source confusion problem. Indeed, the ultra deep survey with the *ROSAT* HRI shows about 80% of the detected sources are type-I AGNs, contradictory to the previous prediction. According to those authors, 10–20% of the total sources could be mis-identified in the deep surveys by *ROSAT* on which we base our estimation. To take this possible mis-identification into account, we have assumed the extreme case, that 20% of the total sources that belonged to other population are actually type-I AGNs. Estimates based on this assumption are presented in parenthesis in columns of Table 6.

For the sample of the 0.7–7 keV and 2–10 keV survey, we can estimate the number density of each population, thus its fraction, by converting the sensitivity limit in each survey band to that in the soft band with assumption of spectra over the 0.7–10 keV range. Note that because the sensitivity limit is determined by the count rate, the flux limit in units of erg s $^{-1}$ cm $^{-2}$ depends on spectra (Table 4), and hence can differ with populations. As for the absolute source counts in the soft band, we adopt our results derived from the LSS to eliminate any possible uncertainty in the mutual calibration between *ROSAT* and *ASCA*.

This estimate is subject to the assumed spectral shape. For the spectrum of type-I AGNs, we as-

sume two cases: a power law with a photon index of 2.0 and 1.6 in the 0.7–10 keV range. Taking these spectra as two extreme limits seems to be reasonable, according to observations of type-I AGNs with *ASCA* at brighter flux levels (George *et al.* 1998; Cappi *et al.* 1997). For clusters of galaxies, we assume a Raymond-Smith plasma model with a temperature of 6 keV, located at a redshift of 0.2, which are typical parameters of clusters observed with *ASCA* (Mushotzky and Scharf 1997). For stars, we assume a power law with a photon index of 3.0 over the 0.7–10 keV range. Since contribution of clusters of galaxies and stars are relatively small, our estimate is not much affected by these assumptions.

The results of our estimates are summarized in Table 6. The fraction of type-I AGNs is estimated to be 45–75% in the 0.7–7 keV survey, and 30–70% in the 2–10 keV survey. Then, the fraction of other population of objects (other than type-I AGN, clusters, or stars) becomes 5–40% in the 0.7–7 keV survey, and 20–60% in the 2–10 keV survey bands, respectively. The corresponding number densities are $N(> S) = 1.5\text{--}12 \text{ deg}^{-2}$ at a flux limit of $7 \times 10^{-14} \text{ erg s}^{-1} \text{ cm}^{-2}$ (0.7–7 keV) and $N(> S) = 3\text{--}9 \text{ deg}^{-2}$ at $1 \times 10^{-13} \text{ erg s}^{-1} \text{ cm}^{-2}$ (2–10 keV). In order to reproduce the observed average spectrum of the LSS sample, which has a photon index of 1.63 ± 0.07 in the 0.7–10 keV range and 1.49 ± 0.10 in the 2–10 keV range, these other population of sources must have hard spectra. We found that the photon index of this population is expected to be 1.1–1.5 in the 0.7–10 keV range and 0.9–1.2 in the 2–10 keV range within the uncertainty range given in Table 6.

We can expect that most of these hard sources are detectable by *ROSAT* with sufficient exposures, knowing their average spectrum calculated above ($\Gamma = 1.1\text{--}1.5$ in the 0.7–10 keV range). To check the consistency of the discussions, we examine here whether the expected number density of these sources can be explained by that of the “other” populations (other than type-I AGNs, clusters, or stars) detected in the *ROSAT* surveys. If we assume a photon index of 1.1 over the 0.5–10 keV range, our sensitivity limit in the 2–10 keV band, $1 \times 10^{-13} \text{ erg s}^{-1} \text{ cm}^{-2}$, corresponds to $2 \times 10^{-14} \text{ erg s}^{-1} \text{ cm}^{-2}$ in the 0.5–2 keV band, which is fainter than the flux limit of the LSS soft-band survey, but brighter than that of the deep surveys with *ROSAT* (Hasinger 1996 and references therein). According to the *ROSAT* results, the number density of the “other” populations is estimated to

be $\sim 8 \text{ deg}^{-2}$ at this flux limit, if their number fraction in the total source counts is 20%. This number density is consistent with that of the hard sources in our survey, 3–9 deg^{-2} at a flux limit of $1 \times 10^{-13} \text{ erg s}^{-1} \text{ cm}^{-2}$ (2–10 keV). This implies that at least a part of *ROSAT* sources that belong to the “other” populations have hard energy spectra over the 0.5–10 keV range.

Good candidates of this population with hard spectra are type-II AGNs (Antonucci and Miller 1985; Awaki *et al.* 1991). Indeed, the hardest source in the LSS was optically identified as a type-II Seyfert galaxy (Akiyama *et al.* 1998), with a heavily absorbed X-ray spectrum (Sakano *et al.* 1998). Preliminary results of on-going optical identification indicate that 20–30% of the hard-band sample are type-II AGNs (Akiyama *et al.* in preparation), which is consistent with the above estimate. From the optical identifications, we find a good correlation that the hard sources correspond to type-II AGNs, which strongly supports our interpretation.

A comparison of our results with the prediction from the population synthesis model proposed by Madau *et al.* (1994) and Comastri *et al.* (1995) would be interesting, where type-II AGNs play an important role to reproduce the CXB. According to Comastri *et al.* (1995), the fraction of type-II AGNs in the total source counts is about 40–50% at a flux of $10^{-13} \text{ erg s}^{-1} \text{ cm}^{-2}$ (2–10 keV). To connect this prediction with our results, however, we must correct for the difference of flux limits for type-I and type-II AGNs that have different spectra. Just to see this effect, we assume a photon index of 1.7 for type-I AGN and 1.0 for type-II AGN in the 2–10 keV range. Then the flux limit for type-II AGNs is brighter than type-I AGNs by about 20% (Table 4), which corresponds to a factor of 30% in the integral source counts assuming a slope of $-3/2$. Thus, the fraction of type-II AGNs in the LSS hard-band sample is predicted to be 30–40%. At present, this is consistent with our estimate, and with the optical identifications, considering uncertainty in the several assumptions we have made. A more detailed study using the optical results will be presented elsewhere.

7. Conclusion

We presented a complete source list in the LSS field, containing 107 sources from the three survey bands of 0.7–7 keV, 2–10 keV, and 0.7–2 keV. Based

on extensive calibration and simulation study, the results are carefully verified. We derived the Log N - Log S relations in each survey band with a flux range of 6×10^{-14} to 8×10^{-13} erg s $^{-1}$ cm $^{-2}$ (0.7–7 keV), 1×10^{-13} to 5×10^{-13} erg s $^{-1}$ cm $^{-2}$ (2–10 keV), and 3×10^{-14} to 2×10^{-13} erg s $^{-1}$ cm $^{-2}$ (0.7–2 keV). At these flux limits, 30(\pm 3)% of the CXB in the 0.7–7 keV and 23(\pm 3)% in the 2–10 keV band have been directly resolved into discrete sources. We found that faint sources around the sensitivity limits show on average a photon index of 1.5 in the 2–10 keV range, and 1.6 in the 0.7–10 keV range. These spectra are harder than a typical spectrum of type-I AGNs, suggesting that contribution of a population with hard energy spectra becomes significant at a flux level of $\sim 10^{-13}$ erg s $^{-1}$ cm $^{-2}$ (2–10 keV). With reasonable assumptions, the fraction of these hard sources is estimated to be 20–60% in the hard band sample. Type-II AGNs are good candidates for this population of sources, which is being confirmed by the on-going optical identifications.

We thank members of the LSS team and the ASCA team for their support in planning observations, satellite operation, and data acquisition. We acknowledge the ASCA-ANL and SimASCA software development teams for supporting the analysis technique. M. S. and M. A. acknowledge the supports from the Japan Society for the Promotion of Science for Young Scientists. We are also grateful to M. Freund for his careful review of the manuscript.

A. Calibration of Instrument Response

Calibration of instrument response, including that of the absolute photometry, is crucial in our study, particularly when we make comparisons with other missions. Here we describe the calibration method and evaluate systematic errors in the instrument response used in the paper.

A.1. GIS+XRT

The response of the GIS and the XRT has been finally determined by the observations of Crab nebula, which is a standard calibration source in X-ray astronomy. Fukazawa, Ishida, & Ebisawa (1997) summarize the results of spectral fits for the Crab data taken at various positions, using the released GIS+XRT responses, which have been tuned especially at the nom-

inal pointing position. They found a tendency that the observed absolute flux increases as the radius from the optical axis becomes large. Although there is no such tendency in the photon index and the column density, the average column density is $N_H \sim 2.5 \times 10^{21}$ cm $^{-2}$, which seems to be somewhat lower than a standard value $((2.7 - 3.3) \times 10^{21}$ cm $^{-2}$, Toor and Seward 1974).

To improve the accuracy of the response further, we corrected it in two practical ways. First, we scaled the effective area of the XRT by an energy-independent factor given as a function of the radius from the optical axis, with a similar formula described in Ishisaki (1996). Second, we modified the low energy efficiency so that a larger column density should be obtained by $N_H = 3 \times 10^{20}$ cm $^{-2}$. Note that this operation is not contradictory to previous calibrations, considering the uncertainty in the low energy response (Ueda 1996).

The fluxes from Crab obtained with the modified response, used throughout in this paper, are plotted in Figure 9 against the radius from the optical axis. As noticed from the figure, the scatter of the flux is less than 8%, which corresponds to the amount of systematic error in relative fluxes observed at different pointings. The average parameters obtained are flux = 2.16×10^{-8} erg s $^{-1}$ cm $^{-2}$ (2–10 keV), photon index = 2.08, and $N_H = 2.8 \times 10^{21}$ cm $^{-2}$, all of which are consistent with the standard values (Toor and Seward 1974). However, we conservatively attach 10% error in the absolute flux, considering the scatter of the flux between different satellites (Seward 1992). Similarly, the systematic error in N_H is estimated to be 3×10^{20} cm $^{-2}$, which produces additional 5% uncertainty in the 0.7–2 keV flux.

A.2. SIS

The degradation of detection efficiency of the SIS, which is prominent in 4 CCD mode, becomes a problem in our study (Dotani *et al.* 1995). This effect is energy independent to first order. To calibrate it, we examined the change of apparent count rate of the CXB spectra using the LSS data taken in different periods, separated by 6 months over 2 years. Since the LSS covers a wide area even in one period, the fluctuation of the CXB surface brightness is almost canceled out after we discard fields where extreme bright sources are located. As expected, we found a clear decrease of the count rate with time. Also, a comparison with the GIS data suggests that even

at December 1993, only 10 months after launch, the absolute detection efficiency in the 4 CCD mode degraded to about 80% relative to that in the 1 CCD mode at launch. We correct this with formula of

$$\begin{aligned} f &= 0.0033 \times t + 0.083 \quad (\text{SIS0}) \\ &= 0.0043 \times t + 0.084 \quad (\text{SIS1}), \end{aligned}$$

where f is detection efficiency normalized by that in the 1 CCD mode at launch, and t is the time in months since the launch. Note that this formula can be applied only for a period of $t = 10 - 28$. The good correlation between the GIS and SIS fluxes in Figure 3 demonstrates the validity of this correction within accuracy of 5%.

REFERENCES

- Akiyama, M., *et al.* 1998, ApJ, 500, 173
- Antonucci, R.R.J. & Miller, J.S. 1985, ApJ, 297, 621
- Awaki, H., Koyama, K., Inoue, H., & Halpern, J.P. 1991, PASJ, 43, 195
- Bower, R., *et al.* 1996, MNRAS, 281, 59
- Burke, B.E., Mountain, R.W., Harrison, D.C., Bautz, M.W., Doty, J.P., Ricker, G.R., & Daniels, P.J. 1991, IEEE Trans. ED-38, 1069
- Butcher, J.A., *et al.* 1997, MNRAS, 291, 437
- Cappi, M. *et al.* 1997, ApJ, 478, 492
- Comastri, A., Setti, G., Zamorani, G., & Hasinger, G. 1995, A&A, 296, 1
- Dotani, T., Yamashita, A., Rasmussen, A., & the SIS team 1995, the *ASCA* News No.3, NASA/Goddard Space Flight Center, p25
- Fabian, A.C., & Barcons, X. 1992, ARA&A, 30, 429
- Forman, M. *et al.* 1978, ApJS, 38, 357
- Fukazawa, Y., Ishida, M., & Ebisawa, K. 1997, the *ASCA* News No.5, NASA/Goddard Space Flight Center, p3
- Gendreau, K.C., *et al.* 1995, PASJ, 47, L5
- Gendreau, K.C., Barcons, X., & Fabian, A.C. 1998, MNRAS, 297, 41
- George, I.M., Turner, T.J., Netzer, H., Nandra, K., Mushotzky, R.F., & Yaqoob, T. 1998, ApJS, 114, 73
- Giacconi, R., Gursky, H., Paolini, F.R., & Rossi, B.B. 1962, Phys. Rev. Lett., 9, 439
- Gioia, I.M. *et al.* 1984, ApJ, 283, 495
- Gioia, I.M. *et al.* 1990, ApJS, 72, 567
- Gotthelf, E. 1996, the *ASCA* News No.4, NASA/Goddard Space Flight Center, p21
- Hasinger, G. 1996, A&AS, 120, 607
- Hasinger, G. 1998, Astro. Nachr., 319, 37
- Hasinger, G., Burg, R., Giacconi, R., Schmidt, M., Trümper, J., & Zamorani, G. 1998, A&A, 329, 482
- Hayashida, K., Inoue, H., & Kii, T. 1990, in proc. of “Frontiers of X-ray Astronomy”, eds. Tanaka, Y. & Koyama, K., p653
- Inoue, H., Kii, T., Ogasaka, Y., Takahashi, T., & Ueda, Y. 1996, in proc. of “Röntgenstrahlung from the Universe”, eds. Zimmermann, H. U., Trümper, J., & Yorke, H., p323
- Ikebe, Y., *et al.* 1997, ApJ, 481, 660
- Ishisaki, Y., Takahashi, T., Kubo, H., Ueda, Y., Makishima, K., & the GIS Team 1995, the *ASCA* News No.3, NASA/Goddard Space Flight Center, p19
- Ishisaki, Y. 1996, Ph.D. thesis, Univ. of Tokyo
- Ishisaki, Y., Ueda, Y., Kubo, H., Ikebe, Y., Makishima, K., & the GIS Team 1997, the *ASCA* News No.5, NASA/Goddard Space Flight Center, p26
- Ishisaki, Y., Makishima, K., Takahashi, T., Ueda, Y., Ogasaka, Y., & Inoue, H. 1999, ApJ, submitted
- Kondo, H. *et al.* 1982, in proc. of “Frontiers of X-ray Astronomy”, eds. Tanaka, Y. & Koyama, K., p655
- Kubo, H., Ikebe, Y., Makishima, K., & the GIS team 1994, the *ASCA* News No.2, NASA/Goddard Space Flight Center
- Kunieda, H., Furuzawa, A., Watanabe, M., & the *ASCA* XRT Team 1995, the *ASCA* News No.3, NASA/Goddard Space Flight Center, p3

- Madau, P., Ghisellini, G., & Fabian, A.C. 1994, MNRAS, 270, L17
- Makishima, K., *et al.* 1996, PASJ, 48, 171
- Marshall, F. *et al.* 1980, ApJ, 235, 4
- Mather, J.C. *et al.* 1994, ApJ, 420, 439
- Nandra, K., & Pounds, K.A. 1994, MNRAS, 268, 405
- McHardy, I.M., Lawrence, A., Pye, J.P. & Pounds, K.A. 1981, MNRAS, 197, 893
- Mushotzky, R.F. & Scharf, C.A. 1997, ApJ, 482, L13
- Ohashi, T., *et al.* 1996, PASJ, 48, 157
- Pfeffermann, E. *et al.* 1986, SPIE, 733, 519
- Piccinotti, G., Mushotzky, R.F., Boldt, E.A., Marshall, F.E., Serlemitsos, P.J. & Shafer, R.A. 1982, ApJ, 253, 485
- Primini, F.A. *et al.* 1991, ApJ, 374, 440
- Sakano, M. *et al.* 1998, ApJ, 505, 129
- Schmidt, M., Hasinger, G., Gunn, J., Schneider, D., Burg, R., Giacconi, R., Lehmann, I., Mackenty, J., Trümper, J., & Zamorani, G. 1998, A&A, 329, 495
- Serlemitsos, P.J., *et al.* 1995, PASJ, 47, 105
- Seward, F. 1992, Legacy No.2, NASA/Goddard Space Flight Center, p47
- Shafer, R.A. & Fabian, A.C. 1983, in proc. of “Early Evolution of the Universe and its Present Structure”, eds. Avell, G.O. & Chincarini, G., p333
- Takahashi, T. *et al.* 1995, the *ASCA* News No.2, NASA/Goddard Space Flight Center, p34
- Takahashi, T., Ueda, Y., Ishisaki, Y., Ohashi, T., & Makishima, K. 1998, Astro. Nachr., 319, 91
- Tanaka, Y., Inoue, H., & Holt, S.S. 1994, PASJ, 46, L37
- Toor, A. & Seward, F.D. 1974, AJ, 79, 995
- Tsusaka, Y. *et al.* 1995, Appl. Opt., 34, 4848
- Turner, T.J. & Pounds, K.A. 1989, MNRAS, 240, 833
- Ueda, Y. 1996, Ph.D. thesis, Univ. of Tokyo
- Ueda, Y., *et al.* 1998, Nature, 391, 866
- Ueda, Y., *et al.* 1999, will appear in *ASCA* News, NASA/Goddard Space Flight Center
- Vikhlinin, A., Forman, W., Jones, C., & Murray, S. 1995, ApJ, 451, 553
- Williams, O.R. *et al.* 1992, ApJ, 389, 157
- Yamashita, A. *et al.* 1997, IEEE Trans. ED-44, 847

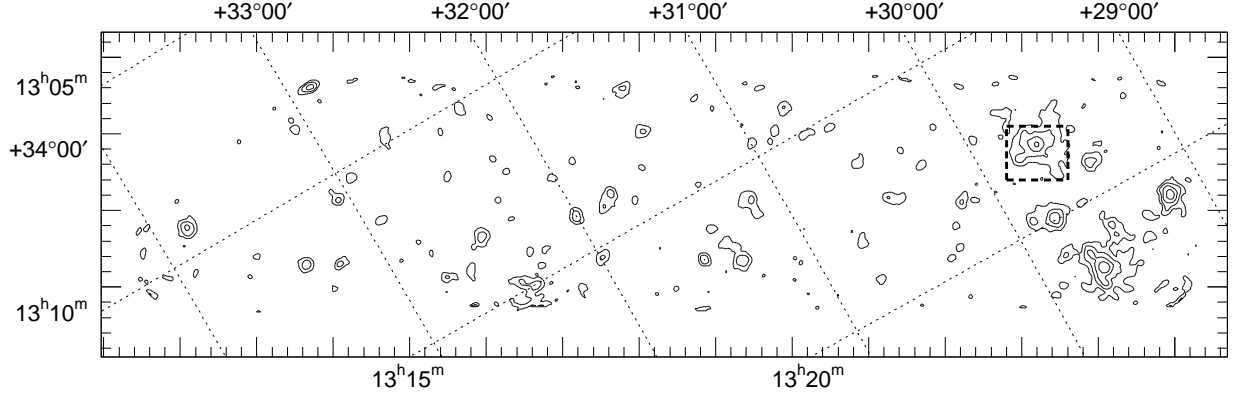


Fig. 1.— The contour plot of the GIS smoothed images of the LSS field in the 0.7–7 keV band obtained by cross-correlating with the position-dependent PSF. The exposure is corrected for each point by dividing with the smoothed exposure map. The rectangle surrounded by dashed lines represents a region where our analysis (Step II; see text) was not performed, to avoid systematic errors due to a bright extended source located there.

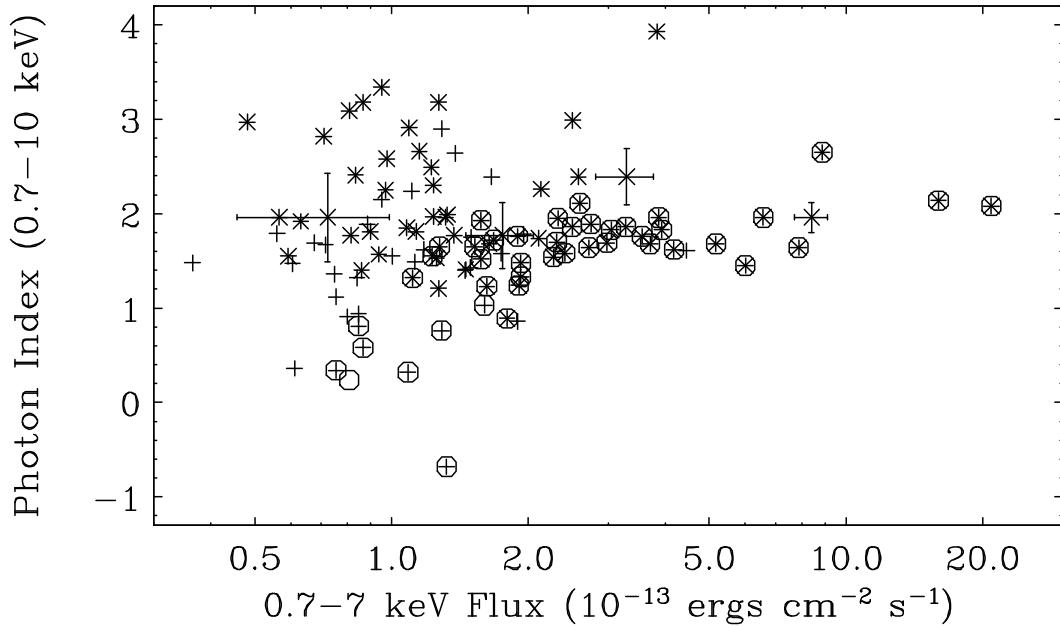


Fig. 2.— Correlation between the flux and the photon index for all the sources detected in the LSS field. Crosses, circles, and diagonal crosses correspond to the detection in the total, hard, and soft band, respectively. The flux is converted from the GIS count rate in the 0.7–7 keV band assuming a photon index of 1.6. Photon indices are determined in simultaneous fitting of the GIS and the SIS spectra in the 0.7–10 keV band with a Galactic absorption fixed at $N_{\text{H}} = 1.1 \times 10^{20} \text{ cm}^{-2}$. The four large crosses show typical 1σ statistical errors.

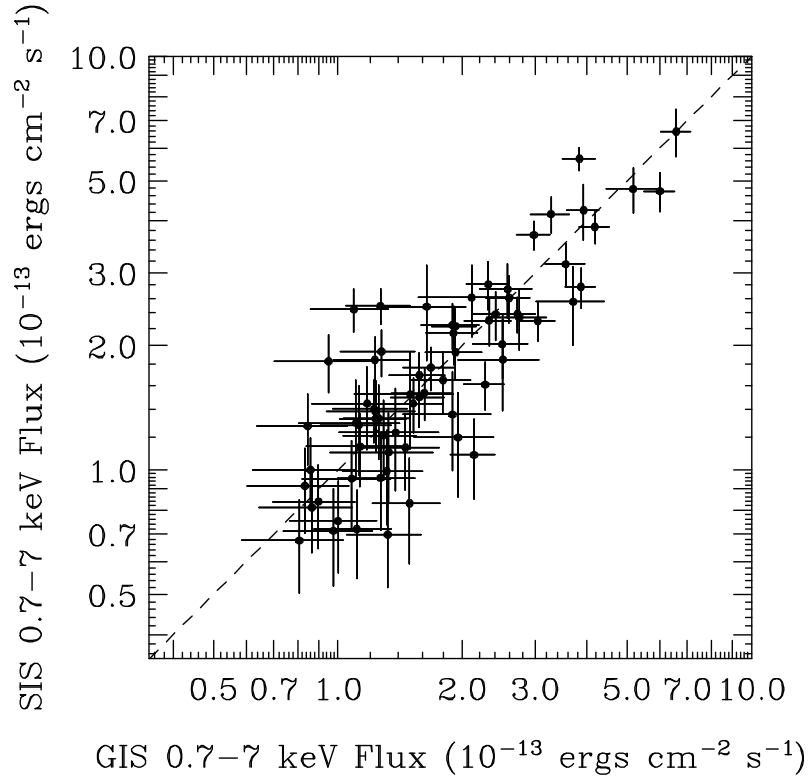


Fig. 3.— Comparison of fluxes between the GIS and the SIS for sources detected both with the GIS and the SIS in the total band (0.7–7 keV). The two fluxes are equal at the dashed line (perfect correlation). A photon index of 1.6 is assumed for conversion from the count rate to the flux. Error bars represent 1σ statistical errors.

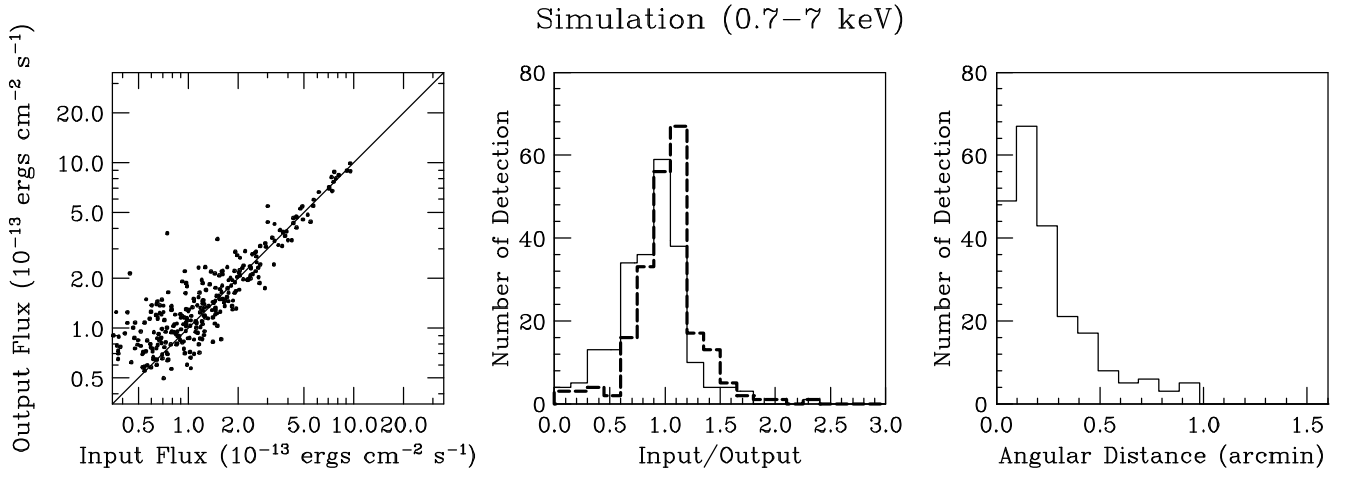


Fig. 4.— (a) Left: comparison between the input and output flux for simulated data generated by our instrument simulator. We applied the same analysis method as for the real data. The input X-ray sky images are created according to the $\text{Log } N - \text{Log } S$ relation obtained in this paper, extending toward a lower flux level with a slope of $-3/2$. The input flux is defined as the flux of the brightest source within a 1 arcmin radius around the detected position. The output flux equals the input flux at the solid line.

(b) Center: histogram of ratio of the input flux to the output flux. The dashed lines correspond to the case that the input flux is defined as an integrated (not the brightest) flux within a radius of 1 arcmin around the detected position.

(c) Right: histogram of angular distance between the detected position and the position of the brightest source within a 1 arcmin radius around the detected position.

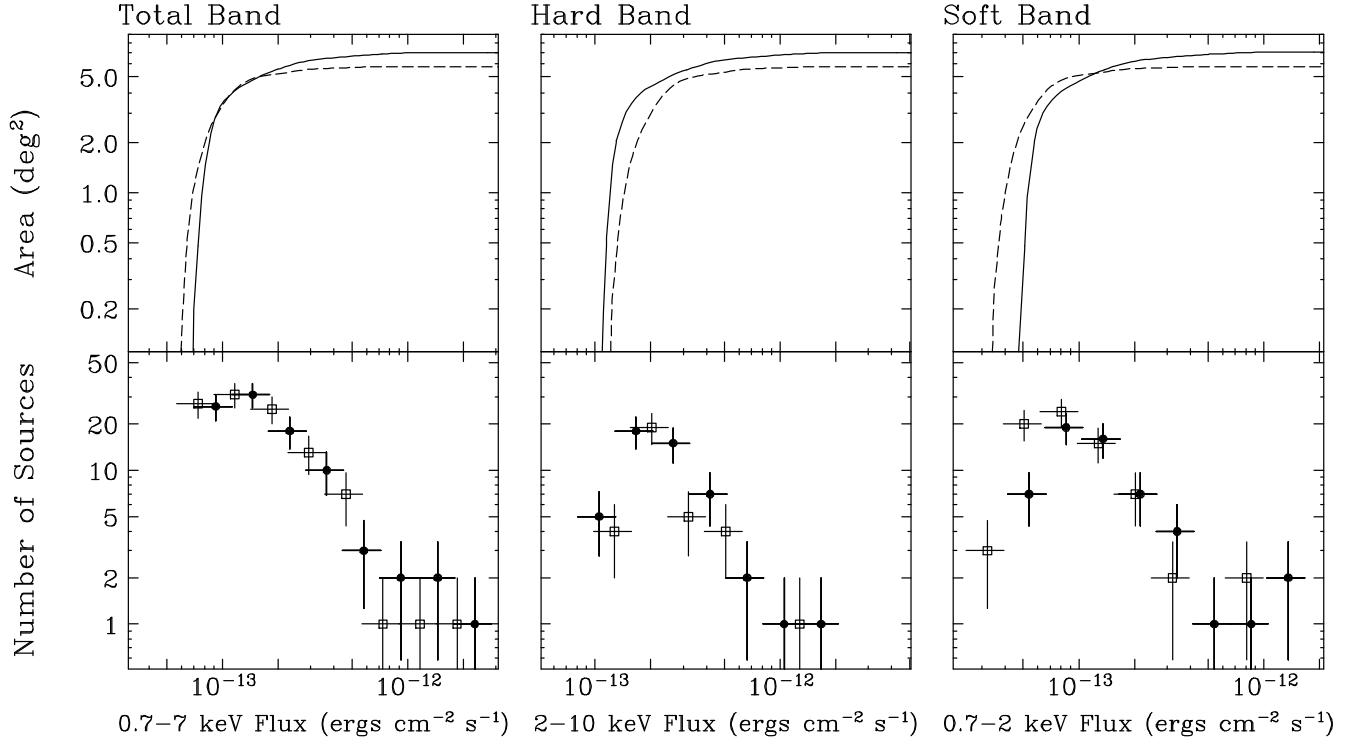


Fig. 5.— (a) Upper: the observed area, Ω , plotted against the sensitivity limit, S , in each survey band. The solid and dashed lines correspond to the GIS and the SIS, respectively. The source detection criteria are $\sigma_g > 3.5$ and $\sigma_t > 3.5$ for the GIS, and $\sigma_s > 3.5$ and $\sigma_t > 3.5$ for the SIS. A photon index of 1.6 (0.7–7 keV), 1.5 (2–10 keV), and 1.9 (0.7–2 keV) is assumed to convert the count rate to flux.

(b) Lower: number of sources detected per unit logarithmic flux bin of width $d \log S = 0.2$. The filled circles and open squares correspond to the GIS and the SIS, respectively.

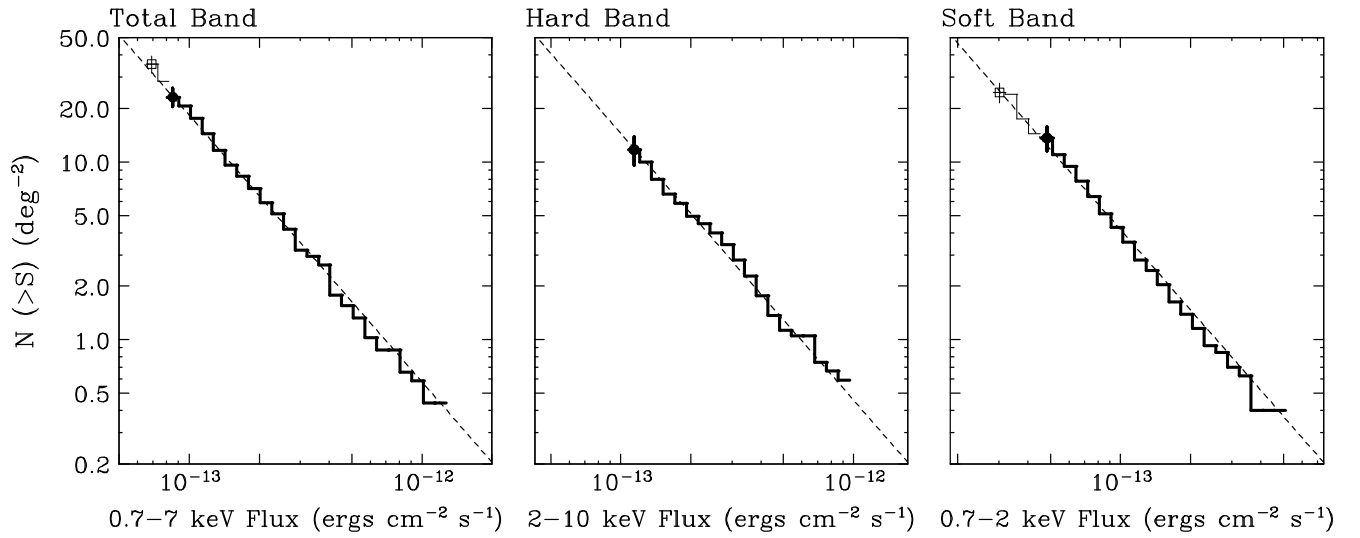


Fig. 6.— The Log N - Log S relations derived from the simulated data. The same analysis method as for the real data is applied. The dashed lines represent the input Log N - Log S relations, which is assumed to extend to the lower flux level with a slope of $-3/2$ until the surface brightness of the CXB is explained. In the 0.7–7 keV and 0.7–2 keV band, the steps with thin lines including the faintest data point (open square) are determined mainly by the SIS.

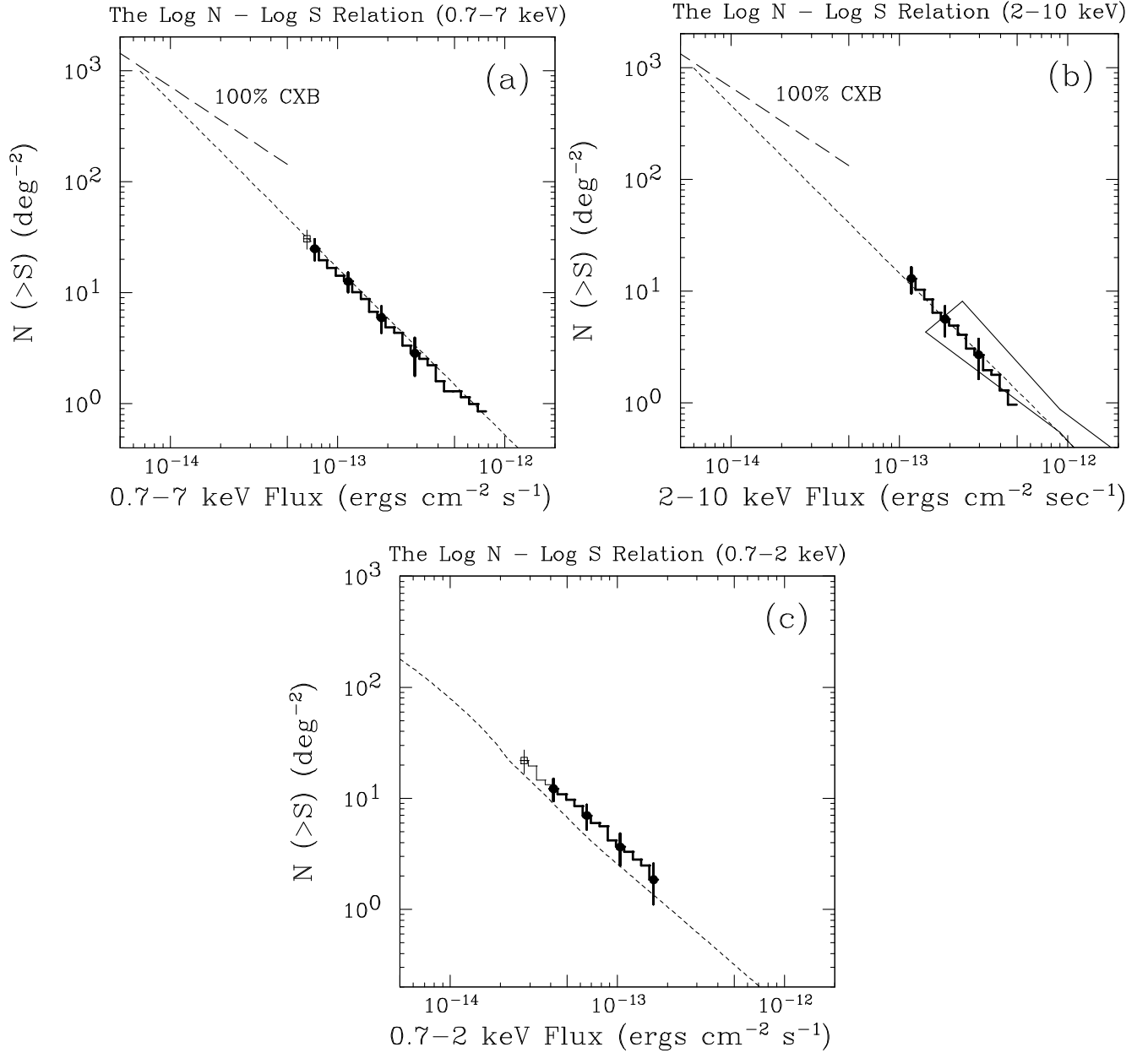


Fig. 7.— The integral Log N - Log S relations in the three energy bands. The steps represent the present results derived from the LSS. The associated systematic errors such as effects of the source confusion were corrected based on the simulation studies (see text). The error attached at several data points, marked with open squares (SIS) or filled circles (GIS), shows a 90% statistical error coming from the Poisson error in the number of detected sources. The long-dashed lines in the 0.7-7 keV and the 2-10 keV band correspond to the condition that the total intensity of the CXB (Ishisaki *et al.* 1998) is explained by the integral of sources assuming $N(> S)$ is proportional to $S^{-3/2}$. For conversion of the count rate to the flux, we assume a photon index of 1.6, 1.5, and 1.9, for the total, hard, and soft bands, respectively. The flux is corrected for the Galactic absorption to give the unabsorbed (emitted) flux.

(a) 0.7-7 keV: the faintest data point (open square) is determined mainly by the SIS and the others are by the GIS. The short-dashed line represents extrapolation with a slope of $-3/2$ from the hard-band source counts by *HEAO1* A2 (Piccinotti *et al.* 1982) by converting the 2-10 keV flux to the 0.7-7 keV flux assuming a photon index of 1.6.

(b) 2-10 keV: all the data points are determined mainly by the GIS. The short-dashed line represents extrapolation with a slope of $-3/2$ from the *HEAO1* A2 result, whose sensitivity limit is 3×10^{-11} erg s $^{-1}$ cm $^{-2}$ (2-10 keV). The contour represents the constraints from the fluctuation analysis by *Ginga* (Hayashida, Inoue, & Kii 1990; Butcher *et al.* 1997).

(c) 0.7-2 keV: the steps with thin lines including the faintest point (open square) are determined mainly by the SIS and the others are by the GIS. The dashed curve shows the *ROSAT* results, converting the flux in the 0.5-2 keV to that in the 0.7-2 keV assuming a photon index of 1.9.

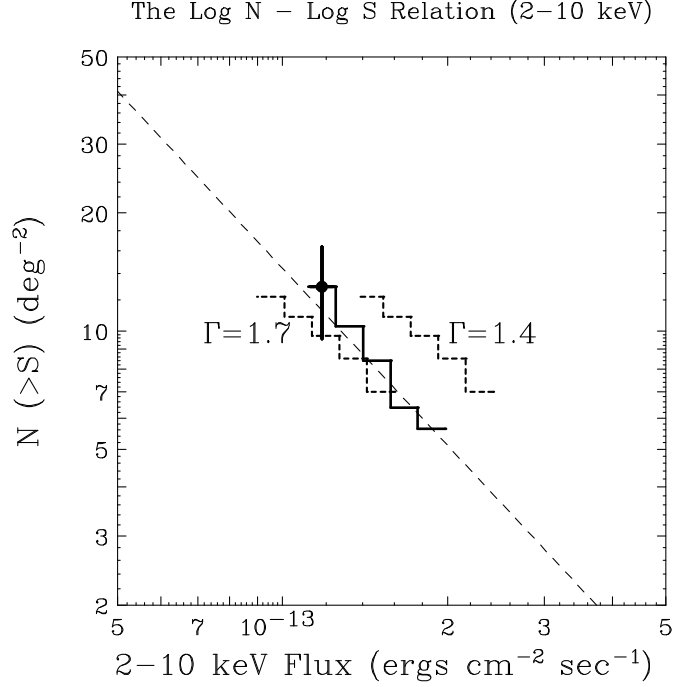


Fig. 8.— Comparison of the Log N - Log S relation between above and below 2 keV derived from the LSS. The steps with thick solid lines represent the Log N - Log S relation in the 2–10 keV band. The steps with dashed lines represent the soft band Log N - Log S relation converted to the hard band flux by assuming two photon indices (1.4 and 1.7). The long dashed line represents extrapolation with a slope of $-3/2$ from the *HEAO1* A2 result.

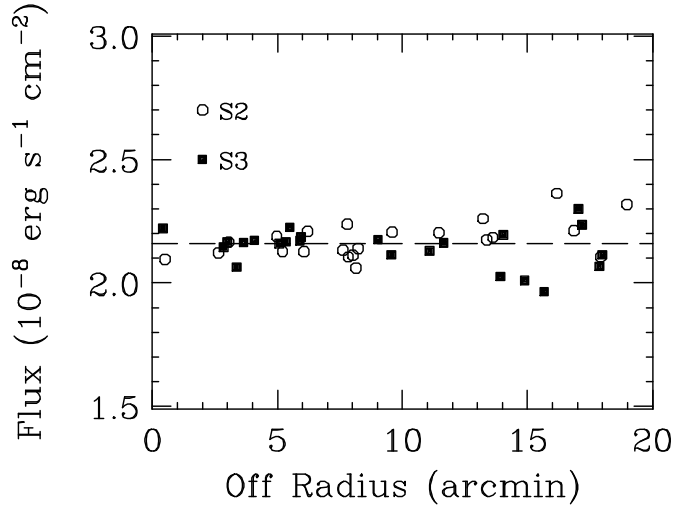


Fig. 9.— The 2–10 keV fluxes of Crab obtained with the GIS+XRT response that is used in this paper from the spectra corresponding to different observing positions, plotted against the radius from the optical axis. Dead time is corrected. Open and filled circles correspond to GIS2 and GIS3, respectively.

TABLE 1
LOG OF THE LSS OBSERVATIONS

Start	End	Pointings	Net Exposure (ksec) ^a
1993/12/26 10:22	1993/12/27 10:00	4	38
1994/01/04 10:32	1994/01/07 19:30	12	122
1994/06/16 16:36	1994/06/19 08:31	10	87
1994/06/27 23:12	1994/06/30 13:20	10	80
1994/12/25 21:35	1994/12/26 13:25	2	18
1995/01/06 08:16	1995/01/06 14:30	1	11
1995/01/07 20:55	1995/01/08 11:10	2	20
1995/01/09 10:54	1995/01/13 07:50	15	147
1995/06/18 16:23	1995/06/20 05:01	5	51
1995/07/01 05:03	1995/07/02 12:51	5	50
1995/07/05 22:13	1995/07/08 11:01	10	97

^aBased on the data selection for the GIS.

TABLE 2
NUMBER OF DETECTED SOURCES

Detection Band	Total	Hard	Soft	One Band Only ^a
Total	105	43	71	27
Hard		44	36	1
Soft			72	1

^aNumber of sources detected only in one band given in the first column

TABLE 3
THE SOURCE LIST IN THE LSS FIELD

Source Name	Position (J2000) ^a		Significance (GIS/SIS) ^b			Count Rate (GIS/SIS) ^{b,c}			Index ^d
	R.A.	DEC.	total (σ)	hard (σ)	soft (σ)	total (c ksec ⁻¹)	hard (c ksec ⁻¹)	soft (c ksec ⁻¹)	Γ
AX J130748+2925	196.9534	29.4328	12.0/7.6	7.0/4.3	9.9/6.3	10.1/17.8	4.2/5.8	6.2/11.9	1.96±0.16
AX J131028+2930	197.6206	29.5120	1.9/5.8	1.6/3.1	1.1/5.0	0.9/5.3	0.6/1.9	0.4/3.4	1.55±0.37
AX J130803+2950	197.0127	29.8435	5.6/4.9	4.4/2.4	3.1/4.4	1.9/3.6	1.2/1.0	0.7/2.6	1.53±0.29
AX J130928+2942	197.3677	29.7066	5.1/4.1	3.3/2.3	3.5/3.4	1.7/3.5	0.9/1.2	0.8/2.2	1.49±0.35
AX J130840+2955	197.1697	29.9242	3.6/3.4	2.9/3.7	1.9/0.9	1.2/2.2	0.8/1.9	0.4/0.4	0.34±0.44
AX J130926+2952	197.3605	29.8670	4.0/5.1	3.9/4.0	1.9/3.3	1.3/3.5	1.0/1.8	0.4/1.6	0.81±0.30
AX J131111+2941	197.7992	29.6880	3.7/3.6	1.1/2.4	4.2/2.6	2.1/3.3	0.4/1.6	1.8/1.7	2.64±0.62
AX J130826+3005	197.1101	30.0946	11.3/6.5	7.0/3.5	8.8/5.6	6.0/11.5	2.7/3.7	3.4/7.8	1.83±0.17
AX J131220+2938	198.0847	29.6360	7.4/—	4.9/—	5.5/—	12.1/—	6.1/—	6.4/—	1.64±0.29
AX J130956+2959	197.4858	29.9883	2.9/4.1	1.2/1.7	3.5/3.8	1.0/2.8	0.3/0.7	0.8/2.1	1.92±0.45
AX J131015+3004	197.5636	30.0720	8.8/7.5	6.2/3.5	6.6/6.7	3.5/7.6	2.0/2.0	1.8/5.6	1.70±0.19
AX J130851+3015	197.2166	30.2505	4.2/3.9	3.6/0.9	2.2/4.1	2.5/6.7	1.8/1.0	0.9/4.9	1.68±0.41
AX J131054+3004	197.7257	30.0689	8.7/7.4	5.2/5.2	7.3/5.4	3.7/6.5	1.7/3.1	2.2/3.4	1.58±0.19
AX J131021+3019	197.5897	30.3280	7.0/6.2	5.3/4.6	4.7/4.2	2.9/5.8	1.8/2.9	1.3/3.0	1.24±0.21
AX J131204+3007	198.0169	30.1191	3.1/3.5	1.9/1.8	2.8/3.2	1.4/2.2	0.6/0.7	0.9/1.6	1.89±0.49
AX J131214+3006	198.0619	30.1071	5.3/3.2	3.9/3.0	3.1/1.7	2.5/2.2	1.4/1.5	0.9/0.8	1.03±0.33
AX J130954+3024	197.4773	30.4079	2.7/3.9	2.4/3.2	1.8/2.4	0.9/3.0	0.7/2.0	0.4/1.2	0.36±0.43
AX J131158+3010	197.9952	30.1754	3.6/5.1	2.9/3.1	2.6/4.0	1.3/2.7	0.8/1.1	0.7/1.6	1.40±0.33
AX J131039+3021	197.6625	30.3585	3.8/6.3	1.0/1.0	4.1/6.5	1.5/5.0	0.3/0.4	1.1/4.3	3.34±0.59
AX J131008+3041	197.5367	30.6883	2.8/4.2	1.1/3.0	2.5/2.9	1.3/3.0	0.4/1.6	0.8/1.5	1.32±0.44
AX J131205+3031	198.0209	30.5185	6.7/6.5	3.9/3.1	5.5/5.8	2.4/4.1	1.0/1.2	1.5/2.9	1.93±0.26
AX J130957+3046	197.4914	30.7812	4.2/3.7	3.8/2.5	2.2/2.8	2.9/3.7	2.2/1.8	0.9/1.9	0.86±0.34
AX J131014+3052	197.5609	30.8693	4.6/3.5	2.3/2.3	4.0/2.7	3.0/3.2	1.1/1.4	1.8/1.9	1.78±0.41
AX J131112+3049	197.8005	30.8292	11.0/15.8	2.1/3.2	12.1/16.0	5.9/15.3	0.6/1.2	5.2/14.0	3.93±0.34
AX J131404+3032	198.5192	30.5481	2.1/4.2	1.4/0.3	1.7/4.3	1.3/4.5	0.8/0.2	0.7/3.7	3.18±1.67
AX J131210+3048	198.0432	30.8025	5.0/4.6	3.8/3.7	2.7/2.7	2.0/3.3	1.2/1.9	0.7/1.4	0.76±0.31
AX J131255+3045	198.2321	30.7659	3.0/6.1	2.9/1.9	2.3/6.6	1.5/4.7	0.8/0.8	0.8/3.6	2.25±0.40
AX J131156+3054	197.9854	30.9120	4.8/7.4	2.5/4.4	4.0/6.0	1.9/5.0	0.7/1.9	1.1/3.0	1.55±0.26
AX J131044+3107	197.6870	31.1330	3.2/3.5	1.3/1.8	3.5/3.1	2.5/3.8	0.7/1.1	1.8/2.7	2.39±0.64
AX J131128+3105	197.8696	31.0953	4.9/7.7	4.0/3.6	2.9/6.9	2.0/5.2	1.3/1.5	0.8/3.7	1.65±0.24
AX J131047+3112	197.6961	31.2098	5.3/4.6	4.8/2.1	2.7/4.2	5.7/6.9	3.9/1.8	1.8/5.1	1.68±0.32
AX J131147+3109	197.9475	31.1591	3.9/5.0	2.0/2.6	2.5/4.4	1.7/3.1	0.7/1.0	0.7/2.1	1.81±0.38
AX J131321+3100	198.3401	31.0082	6.1/5.8	6.0/3.4	2.8/4.8	2.8/4.5	2.3/1.7	0.8/2.8	0.89±0.23
AX J131249+3107	198.2063	31.1195	1.4/4.0	0.0/0.5	1.2/4.5	0.4/2.0	0.0/0.1	0.3/1.9	3.63±1.61
AX J131358+3103	198.4956	31.0540	3.6/4.0	1.9/1.9	3.4/3.6	2.0/3.0	0.8/0.8	1.4/2.0	1.99±0.49
AX J131249+3112	198.2056	31.2165	12.1/11.3	8.2/6.3	8.8/9.4	6.4/10.5	3.3/3.6	3.3/6.9	1.62±0.13
AX J131211+3127	198.0468	31.4515	6.9/6.7	3.2/2.7	5.9/6.2	4.0/7.4	1.3/1.7	2.4/5.7	2.39±0.30
AX J131321+3119	198.3378	31.3250	8.9/7.5	6.8/3.6	6.1/6.7	3.5/4.4	2.1/1.2	1.6/3.1	1.54±0.18
AX J131345+3118	198.4385	31.3063	10.8/12.6	6.8/7.1	8.9/10.3	4.6/10.0	2.2/3.5	2.7/6.5	1.69±0.14
AX J131609+3105	199.0409	31.0868	5.7/—	3.7/—	4.1/—	6.9/—	3.5/—	3.2/—	1.61±0.38
AX J131512+3114	198.8026	31.2444	2.6/3.7	1.4/2.7	2.6/2.6	0.9/1.9	0.4/0.9	0.7/1.0	1.47±0.45
AX J131356+3127	198.4838	31.4625	5.9/3.2	3.2/2.5	5.1/2.1	2.1/1.4	0.8/0.7	1.3/0.7	1.77±0.35
AX J131529+3117	198.8709	31.2924	8.3/7.7	4.1/4.0	7.8/6.5	4.0/7.1	1.4/2.2	2.8/4.8	2.11±0.23
AX J131444+3123	198.6853	31.3891	5.7/10.2	1.5/2.5	6.3/10.3	1.9/6.8	0.3/0.8	1.7/6.0	3.18±0.43
AX J131325+3135	198.3579	31.5953	4.7/8.3	0.8/2.7	5.0/8.2	1.7/6.6	0.2/1.1	1.4/5.6	2.91±0.38
AX J131501+3141 ^e	198.7575	31.6903	4.9/3.9	5.8/4.5	1.1/0.5	2.0/1.9	2.0/1.7	0.2/0.1	-0.68±0.45
AX J131556+3135	198.9855	31.5933	2.7/4.9	1.0/2.4	2.6/4.4	0.9/2.5	0.2/0.7	0.6/1.7	1.96±0.47
AX J131327+3155	198.3634	31.9237	9.1/8.4	6.3/4.1	6.7/7.5	5.5/8.5	2.9/2.3	2.7/6.4	1.76±0.17
AX J131412+3151	198.5506	31.8631	2.7/6.0	1.8/3.2	1.5/5.0	1.4/5.4	0.7/1.9	0.6/3.5	1.57±0.35
AX J131651+3133	199.2156	31.5611	3.7/3.8	2.5/1.9	2.8/3.3	2.3/4.1	1.2/1.2	1.2/2.9	1.75±0.41
AX J131414+3153	198.5616	31.8883	3.3/3.7	0.9/1.3	3.5/3.7	1.8/3.0	0.3/0.7	1.4/2.3	2.66±0.75
AX J131407+3158	198.5302	31.9750	6.3/7.8	3.8/4.3	5.5/6.6	2.9/6.1	1.3/2.1	1.9/4.0	1.76±0.23
AX J131328+3204	198.3688	32.0739	2.6/5.4	1.6/2.9	2.3/4.6	1.2/4.7	0.6/1.5	0.8/3.3	1.77±0.38
AX J131408+3202	198.5350	32.0440	4.1/5.3	1.8/3.2	4.2/4.2	1.9/3.8	0.6/1.4	1.4/2.4	1.97±0.37
AX J131355+3205	198.4801	32.0962	3.9/5.1	2.6/3.2	2.8/4.0	3.2/7.1	1.5/2.6	1.8/4.5	1.74±0.32
AX J131354+3207	198.4769	32.1181	4.5/4.0	1.4/0.7	4.3/4.4	3.9/5.0	0.8/0.4	2.9/4.7	2.99±0.71
AX J131512+3157	198.8022	31.9593	3.8/4.4	2.2/3.0	2.9/3.3	1.8/3.9	0.8/1.6	1.0/2.3	1.62±0.37
AX J131521+3159	198.8392	31.9871	9.3/10.0	6.2/4.7	7.3/8.8	5.0/11.3	2.5/3.0	2.8/8.3	1.86±0.16
AX J131639+3149	199.1634	31.8274	6.9/8.3	4.3/4.6	5.1/6.9	2.6/4.8	1.2/1.6	1.3/3.2	1.72±0.21
AX J131511+3201	198.7981	32.0328	5.3/3.5	3.4/1.9	3.4/3.0	2.3/2.2	1.1/0.7	1.0/1.6	1.43±0.40
AX J131651+3155	199.2147	31.9196	4.7/4.2	3.7/3.0	4.1/3.0	1.7/1.9	1.1/0.9	1.1/1.0	1.32±0.30
AX J131514+3208	198.8085	32.1451	4.1/3.8	1.3/1.8	4.5/3.4	1.5/1.9	0.3/0.5	1.2/1.4	2.58±0.57
AX J131709+3154	199.2908	31.9075	4.6/3.9	3.9/0.5	2.2/4.1	2.0/2.7	1.2/0.2	0.6/2.4	1.96±0.43
AX J131539+3206	198.9138	32.1139	1.7/4.3	2.2/2.2	0.9/3.8	0.6/2.5	0.6/0.8	0.2/1.7	1.48±0.44

TABLE 3—*Continued*

Source Name	Position (J2000) ^a		Significance (GIS/SIS) ^b			Count Rate (GIS/SIS) ^{b,c}			Index ^d
	R.A.	DEC.	total (σ)	hard (σ)	soft (σ)	total (c ksec ⁻¹)	hard (c ksec ⁻¹)	soft (c ksec ⁻¹)	Γ
AX J131742+3152	199.4286	31.8801	6.0/6.0	3.8/2.8	4.8/5.4	4.2/6.3	2.0/1.7	2.3/4.7	1.89±0.27
AX J131522+3218	198.8457	32.3056	4.5/4.4	3.0/1.8	3.5/4.1	1.4/2.3	0.7/0.6	0.8/1.7	1.81±0.37
AX J131724+3203	199.3513	32.0567	6.0/7.0	4.1/4.9	4.1/5.0	2.5/4.2	1.3/1.9	1.2/2.3	1.23±0.22
AX J131638+3211	199.1605	32.1919	3.3/4.1	2.1/2.4	2.9/3.4	1.1/1.9	0.5/0.7	0.7/1.2	1.67±0.42
AX J131650+3222	199.2123	32.3812	3.3/4.4	2.5/2.2	2.0/3.9	1.0/2.4	0.6/0.7	0.4/1.7	1.69±0.41
AX J131526+3234	198.8585	32.5801	3.6/4.3	1.8/1.7	3.4/4.2	1.3/2.5	0.5/0.5	0.9/2.0	2.41±0.47
AX J131742+3220	199.4252	32.3458	3.4/2.6	4.0/2.8	0.0/0.9	1.2/1.3	1.2/1.0	0.0/0.3	0.24±0.54
AX J131730+3222	199.3784	32.3760	8.1/4.5	4.5/0.8	7.1/4.8	3.3/3.0	1.3/0.3	1.9/2.6	2.26±0.30
AX J131551+3237	198.9630	32.6262	3.4/5.5	3.5/5.5	1.3/2.1	1.7/3.1	1.5/2.3	0.4/0.8	0.32±0.34
AX J131735+3225	199.3992	32.4323	3.5/3.3	2.8/2.3	2.7/2.4	1.1/1.7	0.7/0.8	0.6/1.0	1.36±0.40
AX J131707+3237	199.2825	32.6229	7.8/7.6	3.9/3.9	6.1/6.5	3.6/6.2	1.3/1.9	2.0/4.4	1.95±0.24
AX J131821+3232	199.5884	32.5385	5.5/6.0	3.7/1.8	3.7/6.1	1.9/3.6	0.9/0.5	0.9/3.2	2.30±0.34
AX J131621+3248	199.0877	32.8156	3.1/5.5	0.0/2.5	3.6/4.9	1.1/3.4	0.0/0.9	1.0/2.5	2.82±0.53
AX J131816+3240	199.5670	32.6823	8.1/9.3	6.2/5.5	5.2/7.5	3.0/6.0	1.8/2.3	1.3/3.7	1.33±0.16
AX J131918+3238	199.8275	32.6453	4.1/4.2	1.7/3.0	4.0/3.0	1.7/2.6	0.5/1.3	1.2/1.3	1.85±0.42
AX J131725+3300	199.3566	33.0009	6.5/7.6	5.2/4.4	4.1/6.2	2.4/4.6	1.5/1.6	1.0/3.0	1.52±0.21
AX J131654+3304	199.2280	33.0792	4.7/4.0	2.2/2.6	3.6/3.3	1.9/2.6	1.0/1.2	1.0/1.4	1.21±0.32
AX J131758+3257	199.4953	32.9635	9.7/10.2	6.6/5.5	7.0/8.6	4.2/6.5	2.2/2.1	2.1/4.4	1.64±0.15
AX J131928+3251	199.8682	32.8509	5.6/6.6	3.5/3.6	4.0/5.5	2.3/3.9	1.1/1.3	1.1/2.6	1.65±0.26
AX J131813+3301	199.5571	33.0204	3.1/4.0	2.8/3.0	1.5/2.7	1.3/2.3	0.9/1.1	0.4/1.1	0.94±0.38
AX J131832+3259	199.6341	32.9873	3.9/4.5	3.2/4.1	2.1/2.2	1.3/2.2	0.9/1.4	0.5/0.8	0.58±0.35
AX J131812+3303	199.5520	33.0533	2.2/4.0	0.7/2.2	1.9/3.3	0.9/2.1	0.2/0.7	0.5/1.4	1.79±0.54
AX J131844+3306	199.6835	33.1012	3.6/3.9	1.8/2.1	4.0/3.3	1.2/1.8	0.4/0.6	1.0/1.2	3.09±0.50
AX J131905+3303	199.7725	33.0624	3.2/4.0	2.7/2.0	1.2/3.4	1.2/1.9	0.8/0.6	0.3/1.4	1.12±0.28
AX J132011+3257	200.0470	32.9570	3.6/3.7	0.8/2.1	3.6/3.1	1.7/3.5	0.2/1.2	1.3/2.3	2.24±0.62
AX J131904+3308	199.7685	33.1439	4.2/4.0	3.4/2.2	2.8/3.3	1.5/2.0	1.1/0.7	0.7/1.3	1.55±0.22
AX J131842+3311	199.6771	33.1966	3.6/2.9	2.4/0.0	2.7/3.3	1.2/1.3	0.6/0.0	0.6/1.1	0.91±0.31
AX J131831+3320	199.6322	33.3417	10.2/9.6	6.8/5.2	6.5/8.1	4.7/6.2	2.5/2.0	2.0/4.2	1.83±0.11
AX J131850+3326	199.7111	33.4361	20.4/25.8	8.8/9.4	18.6/24.2	13.6/31.7	3.7/5.4	9.7/26.2	2.65±0.09
AX J132104+3309	200.2701	33.1590	3.7/3.2	1.1/1.5	3.9/2.9	2.0/2.7	0.4/0.7	1.6/2.1	2.90±0.81
AX J131808+3335	199.5359	33.5886	6.5/5.7	4.3/2.8	5.2/5.1	3.8/5.5	1.9/1.6	2.2/3.9	1.86±0.26
AX J131928+3330	199.8693	33.5120	4.9/5.8	2.5/2.0	4.9/5.7	1.9/3.8	0.7/0.7	1.4/3.1	2.49±0.39
AX J132032+3326	200.1339	33.4426	12.1/8.9	7.3/4.5	9.7/7.8	6.0/7.5	2.6/2.1	3.4/5.4	1.96±0.16
AX J131831+3341	199.6303	33.6960	11.9/9.4	8.5/5.7	8.4/7.5	9.2/12.8	5.0/4.9	4.6/7.9	1.45±0.14
AX J132054+3328	200.2264	33.4686	1.4/5.1	0.0/1.6	1.4/5.2	0.7/4.3	0.0/0.6	0.6/3.9	2.97±0.70
AX J131805+3349	199.5241	33.8247	7.1/8.0	4.2/5.5	5.0/6.0	8.0/13.0	3.5/5.3	4.4/7.6	1.68±0.21
AX J131935+3338	199.8992	33.6408	3.8/3.2	2.9/0.3	2.1/3.6	1.5/1.7	0.9/0.1	0.5/1.6	2.15±0.57
AX J131822+3347	199.5955	33.7949	25.4/21.6	15.0/10.0	20.4/19.3	32.1/48.9	13.0/11.8	19.2/36.9	2.08±0.07
AX J131927+3343	199.8631	33.7201	6.5/7.3	4.9/4.0	4.5/6.1	3.0/5.2	1.8/1.8	1.4/3.4	1.48±0.21
AX J131917+3345	199.8236	33.7600	4.9/4.8	3.4/2.8	3.4/3.8	2.2/3.1	1.2/1.2	1.1/1.8	1.41±0.31
AX J132010+3351	200.0443	33.8616	4.9/2.3	3.9/1.1	3.2/2.0	2.7/1.7	1.7/0.5	1.2/1.2	1.58±0.37
AX J131939+3355	199.9143	33.9307	4.0/3.1	3.9/0.7	2.1/3.2	2.2/2.7	1.8/0.3	0.8/2.2	1.40±0.40
AX J132055+3354	200.2295	33.9040	11.8/–	6.8/–	9.8/–	24.6/–	9.7/–	15.3/–	2.14±0.20

^aTypical position uncertainty is about 0.7 arcmin in radius (see text).

^b“–” means out of FOV (only for the SIS)

^cVignetting-corrected count rate at the reference position in the XRT coordinate (8'.5 offset for the GIS and 7'.0 offset for the SIS) integrated within a radius of 6' (GIS) and 4' (SIS).

^dThe best-fit photon index obtained by the simultaneous fitting of the GIS and the SIS spectra in the 0.7–10 keV range, assuming a power law with the Galactic absorption ($1.1 \times 10^{20} \text{ cm}^{-2}$). Error is a 1σ statistical error for a single parameter.

^eCorresponds to the LSS hardest source. The position is taken from results of deep X-ray observations by Sakano *et al.* (1998).

TABLE 4
CONVERSION FACTORS FROM COUNT RATE TO FLUX

Assumed Spectrum ^a	Conversion Factor from Count Rate to Flux ^b					
	Total Band ^c		Hard Band ^d		Soft Band ^e	
	Photon Index	GIS	SIS	GIS	SIS	GIS
1.0	0.746	0.478	1.382	1.226	0.408	0.192
1.4	0.678	0.401	1.201	1.033	0.431	0.194
1.5	0.664	0.385	1.161	0.992	0.438	0.194
1.6	0.650	0.369	1.122	0.954	0.444	0.194
1.7	0.638	0.355	1.086	0.918	0.451	0.195
1.8	0.628	0.341	1.051	0.884	0.458	0.195
1.9	0.618	0.329	1.018	0.853	0.465	0.196
2.0	0.610	0.317	0.986	0.823	0.472	0.196
3.0	0.592	0.246	0.751	0.615	0.561	0.202

^aA Galactic absorption of $N_{\text{H}} = 1.1 \times 10^{20} \text{ cm}^{-2}$ is assumed.

^bIn units of $[10^{-13} \text{ erg s}^{-1} \text{ cm}^{-2}] / [\text{count ksec}^{-1}]$. The count rate is the vignetting-corrected count rate given in the source list (Table 3). Flux is corrected for the Galactic absorption (i.e., unabsorbed flux).

^cFrom 0.7–7 keV count rate to 0.7–7 keV flux

^dFrom 2–10 keV count rate (2–7 keV for SIS) to 2–10 keV flux

^eFrom 0.7–2 keV count rate to 0.7–2 keV flux

TABLE 5
AVERAGE SPECTRA FOR FLUX LIMITED SAMPLES

Sample			Best Fit Photon Index ^a	
Survey Band	Flux Range ($10^{-13} \text{ erg s}^{-1} \text{ cm}^{-2}$)	Number of Sources	Fitting Range 0.7–10 keV	2–10 keV
Total	0.5–2.0 (0.7–7 keV)	74	1.63 ± 0.07	1.63 ± 0.18
Hard	0.8–4.0 (2–10 keV)	36	$(1.51 \pm 0.05)^{\text{b}}$	1.49 ± 0.10
Soft	0.3–3.0 (0.5–2 keV)	64	$(1.76 \pm 0.07)^{\text{b}}$	1.85 ± 0.22

^aA Galactic absorption of $N_{\text{H}} = 1.1 \times 10^{20} \text{ cm}^{-2}$ is assumed. The error indicates 1σ statistical error for a single parameter.

^bThis value could be affected by statistical bias (see text).

TABLE 6
ESTIMATION OF NUMBER FRACTION OF POPULATIONS IN OUR SAMPLE

Population	Assumed Spectrum	Expected Percentage in the Sample ^a		
		0.7–7 keV	2–10 keV	0.7–2 keV ^b
AGN	$\Gamma = 2.0^c$	45 (65)	30 (40)	60 (80)
	$\Gamma = 1.6^c$	55 (75)	50 (70)	60 (80)
CG	$kT = 6^d$	10	10	10
Star	$\Gamma = 3.0^c$	5–10	<2	10–15
Other ^e		25–40 (5–20)	50–60 (20–50)	15–20 (0)

^aThe parenthesis indicates an extreme case under the possible uncertainty in the identifications of the *ROSAT* sources (see text).

^bThe estimation in the soft band is made based on the results by *ROSAT* in the 0.5–2 keV band (Hasinger 1996 and references therein).

^cPower law photon index.

^dTemperature in keV for a Raymond-Smith plasma model with an elemental abundance of 0.3 solar value and a redshift of 0.2.

^e Includes NELGs and unidentified objects in the *ROSAT* surveys.